# How Bright in Gravitational Waves are Millisecond Pulsars for the Galactic Center GeV Gamma-Ray Excess? A Systematic Study

Ming-Yu Lei  $,^{1,2}$  Bei Zhou  $\bigcirc ,^{3,4,*}$  and Xiaoyuan Huang  $\bigcirc ,^{1,2,\dagger}$ 

<sup>1</sup>Key Laboratory of Dark Matter and Space Astronomy, Purple Mountain Observatory, Chinese Academy of Sciences, Nanjing 210023, China <sup>2</sup>School of Astronomy and Space Science, University of Science and Technology of China, Hefei 230026, China <sup>3</sup>Theory Division, Fermi National Accelerator Laboratory, Batavia, Illinois 60510, USA <sup>4</sup>Kavli Institute for Cosmological Physics, University of Chicago, Chicago, Illinois 60637, USA (Dated: November 21, 2025)

The existence of dark matter (DM) is supported by various macroscopic observations, but its microscopic nature remains elusive. The Galactic Center GeV gamma-ray excess (GCE) has been a leading candidate signal for particle dark matter annihilation. However, an unresolved population of millisecond pulsars (MSPs) in the bulge provides the alternative explanation for the excess. Identifying these MSPs in electromagnetic bands is difficult due to source confusion, pulse broadening. and extinction. Gravitational waves (GWs) provide a complementary probe: a steadily rotating, non-axisymmetric MSP emits a nearly monochromatic GW signal in the sensitive band of groundbased detectors, with amplitude set by its ellipticity. In this work, we systematically investigate the GW emission from the MSP population proposed to explain the GCE and its detectability with current and future detectors. We consider three major scenarios for the origin of ellipticity and model the population properties of these MSPs. We also consider both isolated MSPs and MSPs in binary systems, as well as Doppler effects in the detection. We find that while the signal is below the reach of current interferometers, next-generation detectors such as the Einstein Telescope (ET) and Cosmic Explorer (CE) can detect a fraction of those MSPs, offering a novel test of the MSP interpretation of the GCE. Future directed searches toward the Galactic Center with continued improvements in sensitivities will either uncover this long-sought MSP population or place stringent limits on their ellipticities and abundance, with important implications for both the astrophysical and dark-matter interpretations of the GCE.

#### I. INTRODUCTION

The existence of dark matter is supported by a broad set of macroscopic observations, including galaxy rotation curves [1–3], lensing in clusters (including the Bullet Cluster) [4, 5], large-scale structure [6, 7], and precision measurements of the cosmic microwave background [8, 9]. Despite this breadth of macroscopic evidence and an increasingly precise determination of the cosmic DM abundance, the microscopic nature of DM remains unknown: no experiment has yet identified the particle(s) that constitute DM or measured their interactions beyond gravity [10–12]. Worldwide experiments conducting direct, indirect, and collider searches continue to narrow viable parameter space across many candidate frameworks (e.g., WIMPs, axions, sterile neutrinos), but no conclusive signal has been established [13–23].

The GCE has been a leading candidate signal for particle DM. It is characterized by a bump spectrum centered around 2 GeV with a several-GeV width and a roughly spherically symmetric morphology extending several degrees around the Galactic Center (GC). It was first identified and interpreted as a possible signature of dark matter annihilation in Ref. [24], and its robustness against uncertainties in galactic diffuse fore-

ground modeling was subsequently confirmed in multiple independent analyses [25–34]. A variety of particle-DM models have been invoked to explain the GCE [35–41], most prominently weakly interacting massive particles (WIMPs) with masses of a few tens of GeV annihilating predominantly into  $b\bar{b}$ , which hadronize and decay to gamma rays.

However, there is also a well-motivated astrophysical interpretation: an unresolved population of MSPs in the inner Galaxy can reproduce the observed GCE spectrum and morphology at current Fermi-LAT resolution [42–49]. These MSPs are mostly in the Galactic bulge, so hereafter we refer to them as "bulge MSPs" for simplicity. MSPs are rapidly rotating neutron stars (NSs) whose rotational kinetic energy can power radio, gamma rays, and other electromagnetic emissions. Young pulsars spin down on Myr timescales; subsequent accretion can recycle "dead" pulsars to millisecond periods [50]. These recycled MSPs typically have lower surface magnetic fields,  $B_{\rm surf} \sim 10^8$ – $10^9$  G, and their long lifetimes of order Gyr make the existence of a substantial bulge population astrophysically plausible [51–56].

Identifying these bulge MSPs would provide a direct way to distinguish the DM and MSP interpretations of the GCE. However, resolving these sources across electromagnetic bands remains challenging, and only one candidate, PSR J1744-2946 [57], has been tentatively identified so far. In gamma rays, most bulge MSPs are too faint to resolve individually, and the ~degree-scale point-spread

<sup>\*</sup> beizhou@fnal.gov

<sup>†</sup> xyhuang@pmo.ac.cn

function at GeV energies leads to severe source confusion [58]; only a few candidates have been discussed, and none are confirmed [59, 60]. In radio, the detectability of bulge MSPs is limited by both strong multipath scattering, which broadens pulsar signals and makes timing searches difficult, and bright foreground emission in the Galactic plane [61–63]. In UV/optical/near-IR, extinction toward the GC is substantial and isolated MSPs are intrinsically faint. Analyses of static X-ray properties (e.g., flux and spectra), combined with multiwavelength data, can identify promising MSP candidates in the Galactic bulge [64, 65]. However, such methods do not yield timing information; confirmation still relies on targeted pulse searches to detect the characteristic pulsations.

GWs provide a complementary probe that is insensitive to dust, scattering, and the source-confusion problems in the crowded stellar fields around the GC. A steadily rotating, non-axisymmetric neutron star emits a continuous, nearly monochromatic GW signal at  $f_{\rm GW} \simeq 2f_{\rm rot}$ , typically in the  $\simeq 200-2000$  Hz range for MSPs, which coincides with the most sensitive band of ground-based interferometers [66], including LIGO [67], Virgo [68], KAGRA [69], and next-generation CE [70] and ET [71]. Although it is very difficult to resolve the large number of MSPs in the crowded bulge region using gamma rays and other electromagnetic wavelengths, GWs can potentially resolve individual MSPs in the frequency domain, thanks to a resolution of  $\Delta f \sim 1/T_{\rm obs}$ .

Building upon the previous work [72–74], we present a refined analysis that incorporates a more physically motivated signal prediction and a detailed treatment of the detector response. This allows us to investigate the GW emission expected from the MSP population responsible for the GCE and assess its detectability with present and future ground-based GW interferometers [75]. The GW emission arises from a finite ellipticity, and we consider major physically motivated scenarios that can generate such ellipticities: (1) internal magnetic-field-induced deformation, (2) long-lived crustal mountains from breaking strain, and (3) a general parametrization in terms of a fraction of the pulsar spin-down energy. Importantly, the third scenario also naturally yields a theoretical maximum, assuming all the spin-down power is converted to GW emission. We model the bulge MSPs by combining a fixed boxy bulge morphology, constrained by the GCE, with two distinct population frameworks, an Empirical Disk-Proxy Model and an Evolutionary Model, which respectively benchmark and selfconsistently derive the necessary intrinsic MSP parameters and total population size. For detectability, we outline two search strategies—coherent and incoherent that explicitly account for Doppler shifts from Earth's motion and binary orbits. Our results demonstrate that, under conservative assumptions, the bulge MSPs can produce GW signals approaching the sensitivity of nextgeneration ground-based interferometers, such as CE and the ET [76, 77]. For the theoretical maximum, a fraction

of MSPs can reach the LIGO-Virgo-Kagra (LVK) O4 sensitivity [78, 79].

This paper is organized as follows. In Sec. II, we discuss the continuous GW emission from MSPs and define the key quantities used throughout. In Sec. III, we present three major scenarios for the origin of MSPs' ellipticity. In Sec. IV, we describe the bulge MSP population models, including intrinsic parameters and spatial morphologies. We also discuss the total number of bulge MSPs in light of the GCE. In Sec. V, we discuss the detection of MSPs' GW signals, including the Doppler shifts in frequency, and outline two search strategies: coherent and incoherent. In Sec. VI, we present our results, including their GW strain amplitude and detectability in current and next-generation GW detectors. We conclude in Sec. VII.

#### II. GW EMISSIONS FROM MSPS

To estimate the GW signals from MSPs, we adopt the standard quadrupolar emission formula, assuming a steadily rotating, non-axisymmetric rigid neutron star, with a constant ellipticity, radiating in the far field under the linearized theory of general relativity [80]. These are well-motivated and widely used assumptions. Accordingly,

$$h_{+} = h_{0} \frac{1 + \cos^{2} \iota}{2} \cos(2\pi f_{\text{GW}} t),$$
  
 $h_{\times} = h_{0} \cos \iota \sin(2\pi f_{\text{GW}} t),$  (1)

where

$$h_0 = \frac{4\pi^2 G}{c^4} \frac{I_{zz} f_{\text{GW}}^2}{r} \epsilon.$$
 (2)

Here,  $h_+$  and  $h_\times$  are the two GW polarization amplitudes,  $\iota$  is the inclination angle between the MSP's rotation axis and the line of sight,  $f_{\rm GW}$  is the GW frequency (twice the pulsar's rotational frequency,  $f_{\rm rot}$ ), G is Newton's gravitational constant, c is the speed of light,  $I_{zz}$  is the moment of inertia about the rotation axis, r is the distance to the pulsar, and  $\epsilon$  is the equatorial ellipticity, with

$$\epsilon \equiv \frac{I_{xx} - I_{yy}}{I_{zz}} \,, \tag{3}$$

i.e., the fractional difference between the two moments of inertia orthogonal to the rotation axis.

NSs typically have a mass of  $m_{\rm NS} \simeq 1.4 M_{\odot}$  and a radius of  $R_{\rm NS} \simeq 12$  km, which gives  $I_{zz} \simeq (2/5) m_{\rm NS} R_{\rm NS}^2 \simeq 1.6 \times 10^{38} \, {\rm kg \, m^2}$ . As a result,

$$h_0 \simeq 2.1 \times 10^{-27} \left(\frac{\epsilon}{10^{-8}}\right) \left(\frac{m_{\rm NS}}{1.4 M_{\odot}}\right) \left(\frac{R_{\rm NS}}{12 \,\mathrm{km}}\right)^2 \times \left(\frac{8.178 \,\mathrm{kpc}}{r}\right) \left(\frac{f_{\rm GW}}{1 \,\mathrm{kHz}}\right)^2. \tag{4}$$

#### III. ORIGINS OF MSPS ELLIPTICITY

A key parameter governing the emission of continuous GWs from MSPs is the stellar ellipticity,  $\epsilon$ . This quantity describes the deviation of the NS from perfect axisymmetry. In this work, we explore three distinct scenarios: (1) ellipticity generated by stresses from strong internal magnetic fields within the NS; (2) ellipticity arising from non-axisymmetric crustal deformations ("crustal mountains") that become permanently frozen in as the NS cools and the solid crust forms; (3) a model-independent parametrization in which GW emission accounts for a fraction  $\eta$  of the total spin-down energy. In this work, we adopt  $\eta=1\%$  as a benchmark value. Importantly, this scenario provides a theoretical maximum when  $\eta=100\%$ , i.e., GW emission accounts for all the spin-down power.

Previous work by Woan et al. [81], using MSP data available up to 2018, suggested that MSPs may sustain a minimum ellipticity at the level of  $\sim 10^{-9}$ . However, this conclusion is derived from the existing MSP observations and may be influenced by the observational selection effect. The confirmation of additional MSPs exhibiting short rotation periods and extremely low period derivatives, beyond the two already documented in Ref. [81], would challenge the current hypothesis. Thus, we do not apply a minimum ellipticity in our calculations.

This section focuses on the physical origins of ellipticity in individual MSPs. The application of these models to the MSP population in the bulge, including the resulting ellipticity distributions, is discussed in Sec. IV.

#### A. Magnetic-Field-Induced Deformation

A strong internal magnetic field within an NS can induce a non-axisymmetric deformation. If the axis of the internal magnetic field,  $B_{\rm int}$ , is misaligned with the star's rotation axis, the resulting magnetic pressure is anisotropic, distorting the star from a perfect spheroid [82, 83]. Theoretical estimates also suggest that the protons in the NS core form a type II superconductor [84, 85]. In such a state, the internal magnetic field is confined to quantized flux tubes. The tension from these flux tubes creates an anisotropic stress that deforms the star. This magnetic-field-induced deformation results in an ellipticity that scales linearly with the internal magnetic field strength,  $B_{\rm int}$  [86–90]:

$$\epsilon \approx 10^{-8} \left( \frac{B_{\rm int}}{10^{12} \text{ G}} \right). \tag{5}$$

While the internal magnetic field,  $B_{\rm int}$ , cannot be directly observed, it is commonly inferred from the measured external surface dipolar magnetic field  $B_{\rm surf}$ . The ratio of  $B_{\rm int}$  to  $B_{\rm surf}$  is expected to be  $\sim 10^2$  to  $10^4$  for MSPs [91–93]. Consistent with previous studies [73, 74], we adopt a conservative benchmark ratio for this work:

$$B_{\rm int} = 150 B_{\rm surf}. \tag{6}$$

The surface magnetic field can be inferred from the observed period (P) and its derivative  $(\dot{P})$ . We move beyond the simple vacuum dipole approximation, which is insufficient for the plasma-filled environments of pulsars, and adopt a relation derived from the braking torque in a force-free magnetosphere model [94]. The surface magnetic field is thus given by:

$$B_{\rm surf}^2 = \frac{3c^3 I_{zz} P\dot{P}}{5\pi^2 R_{\rm NS}^6},\tag{7}$$

where  $I_{zz}$  is the moment of inertia and we assume a canonical NS radius  $R_{\rm NS}=12$  km. Combining these relations, we obtain a scaling for the ellipticity as a function of the observable MSP parameters:

$$\epsilon \simeq 2.7 \times 10^{-10} \left( \frac{f_{\rm rot}}{300 \text{ Hz}} \right)^{-\frac{3}{2}} \left( \frac{\left| \dot{f}_{\rm rot} \right|}{10^{-15} \text{ Hz s}^{-1}} \right)^{\frac{1}{2}} \times \left( \frac{m_{\rm NS}}{1.4 M_{\odot}} \right)^{\frac{1}{2}} \left( \frac{12 \text{ km}}{R_{\rm NS}} \right)^{2},$$
(8)

where  $f_{\rm rot}$  and  $\dot{f}_{\rm rot}$  are the rotational frequency and its first time derivative, and  $m_{\rm NS}$  is the NS mass.

#### B. Crustal Mountains from Breaking Strain

As a newly formed neutron star cools, its outer layers crystallize into a solid crust. This crust solidifies in an equilibrium shape corresponding to the star's rapid initial rotation. As the NS spins down, the hydrostatic equilibrium shape gradually evolves, while the rigid crust resists the deformation. Stress therefore accumulates until the energy difference between the new equilibrium shape and the actual crust configuration becomes sufficiently large that the crust can no longer withstand it. At this point, the crust breaks down and adjusts to the new equilibrium. This scenario provides a natural mechanism for generating a non-axisymmetric ellipticity in the NS [95–98].

In the extremely ideal scenario, if the whole crust reaches the breaking strain, the maximum ellipticity is reached at

$$\epsilon^{\text{ideal}} < 4 \times 10^{-6} \left( \frac{u_{\text{break}}}{0.1} \right),$$
(9)

where  $u_{\text{break}}$  is the crustal breaking strain (distinct from the "strain" in GW detection), and is  $\sim 0.1$  determined from molecular-dynamics simulations of Coulomb solids representative of the NS crust [99].

In practice, however, only localized regions of the crust reach stresses close to the breaking strain. As a result, the typical initial ellipticity is expected to be significantly smaller than the theoretical maximum, at the level of

$$\epsilon^{\text{initial}} \sim 10^{-8} \text{ to } 10^{-7}.$$
(10)

Over longer timescales, plastic flow and viscoelastic creep gradually relax these deformations [100], reducing the ellipticity to a long-term residual value of [101]

$$\epsilon \sim 10^{-9} \,, \tag{11}$$

which can last for gigayears and is the realistic target for GW emission from MSPs. This expectation is consistent with recent results indicating that a slightly anisotropic neutron star crust, undergoing modest changes in rotation rate, can support an ellipticity of a few  $\times 10^{-9}$  [102], comparable to the observational upper bounds inferred for some nearby and rapidly spinning pulsars [103].

Therefore, we adopt a constant typical ellipticity of  $\epsilon = 10^{-9}$ . This is independent of MSPs' parameters.

## C. Model-Independent Spin-Down Energy Fraction

We also consider a more model-independent way to parametrize the ellipticity by simply assuming that a fraction,  $\eta$ , of the spin-down energy loss goes into GW emission.

The ellipticity in this scenario can be solved as follows. The rotational energy loss due to GW emission is given by [80]

$$\eta \frac{\mathrm{d}E_{\mathrm{rot}}}{\mathrm{d}t} = -\frac{32G}{5c^5} \epsilon^2 I_{zz}^2 \omega_{\mathrm{rot}}^6 \,, \tag{12}$$

where  $\omega_{\rm rot} \equiv 2\pi f_{\rm rot}$ . The rotational energy of an NS about its principal axis  $x_{zz}$  is expressed as  $E_{\rm rot} = (1/2)I_{zz}\omega_{\rm rot}^2$ . This leads to

$$\epsilon = \sqrt{\frac{5c^5}{2G} \frac{|\dot{f}_{\rm rot}|}{I_{zz} f_{\rm rot}^5}} \cdot \frac{1}{16\pi^2} \cdot \sqrt{\eta}. \tag{13}$$

Here, the  $f_{\text{rot}}$  and  $\dot{f}_{\text{rot}}$  denote the pulsar's rotational frequency and its time derivative, respectively.

We adopt  $\eta=1\%$  as our benchmark. Plugging in the other typical numbers, we obtain the scaling of  $\epsilon$  with MSPs' parameters

$$\epsilon \simeq 3.1 \times 10^{-10} \left( \frac{\eta}{0.01} \right)^{1/2} \left( \frac{f_{\rm rot}}{300 \,\text{Hz}} \right)^{-5/2} \left( \frac{\left| \dot{f}_{\rm rot} \right|}{10^{-15} \,\text{Hz/s}} \right) \times \left( \frac{1.4 M_{\odot}}{m_{\rm NS}} \right)^{1/2} \left( \frac{12 \,\text{km}}{R_{\rm NS}} \right)$$
(14)

Importantly, a **theoretical maximum** on  $\epsilon$  can be naturally set in this scenario from the **spin-down limit**, i.e., assuming all ( $\eta = 100\%$ ) the spin-down energy is taken away by GW emission:

$$\epsilon^{\text{max}} \simeq 3.1 \times 10^{-9} \left( \frac{f_{\text{rot}}}{300 \text{ Hz}} \right)^{-5/2} \left( \frac{\left| \dot{f}_{\text{rot}} \right|}{10^{-15} \text{ Hz/s}} \right)^{1/2} \times \left( \frac{1.4 M_{\odot}}{m_{\text{NS}}} \right)^{1/2} \left( \frac{12 \text{ km}}{R_{\text{NS}}} \right).$$
(15)

# IV. POPULATION PROPERTIES OF BULGE MSPS

In this section, we discuss the population properties of the bulge MSPs that determine their GW detectability. In Sec. IV A, we discuss the distributions of the intrinsic parameters of MSPs in the bulge, including magnetic field strength (B), rotational frequency  $(f_{\rm rot})$  and its time derivative  $(\dot{f}_{\rm rot})$ , which are directly related to the period (P) and its derivative  $(\dot{P})$ . These parameters, in conjunction with the discussion in Sec. III, determine the ellipticity distributions of bulge MSPs, as shown in Sec. IV B. In Sec. IV C, we discuss the morphological distribution, as the distances to the MSPs affect their GW detectability. Finally, in Sec. IV D, we estimate the total number of bulge MSPs,  $N_{\rm MSP}$ , as constrained by their gamma-ray luminosity and the observed GCE luminosity.

# A. Models for MSP Population Parameters

A statistically significant population of MSPs has yet to be individually resolved in the bulge. Therefore, inferring the properties of this putative population requires model-based approaches, for which we explore two primary, physically distinct frameworks. The first is the Empirical Disk-Proxy Model (Pop. I), which assumes the bulge MSPs share the same present-day properties as the well-characterized population in the Galactic disk, with fiducial distributions derived from the Australian Telescope National Facility (ATNF) pulsar database [104]. The second framework is the Evolutionary Model (Pop. II), which is a theoretical approach informed by the work of Ploeg et al. [59]. It interprets the GCE as originating from an older MSP population native to the bulge, allowing for a self-consistent derivation of its evolved properties (e.g., longer periods, lower luminosities) from universal birth parameters and the region's specific star formation history [105]. While the Pop. II provides a direct fit to the observed GCE, its predicted number of MSP, discussed in Sec. IVD, exhibits mild tension with a recent machine learning analysis of the GCE [106], which favors a lager MSP population with  $N_{\rm MSP} > 10^5$ .

We first construct the Pop. I by deriving distributions for the rotational frequency  $(f_{\rm rot})$  and its derivative  $(\dot{f}_{\rm rot})$  from the ATNF pulsar catalog [104]. To curate a clean and representative sample, we apply the selection cuts that canonical pulsars are removed via a rotational frequency cut  $(f_{\rm rot} > 100~{\rm Hz})$  [81]. Crucially, we filter the catalog to remove sources with a measured spin-up  $(\dot{f}_{\rm rot} > 0)$ . Such sources are typically found in globular clusters, where local dynamical effects, such as acceleration within the cluster's gravitational potential, can induce an apparent spin-up that masks the intrinsic spin-down rate [107, 108]. This filtering yields a cleaner sample from which to infer the true spin-down properties of the Galactic disk population. In version 2.6.5 of the

ATNF pulsar catalog, a total of 673 MSPs satisfy the criterion  $f_{\rm rot} > 100$  Hz, of which 54 exhibit  $\dot{f}_{\rm rot} > 0$ . After excluding these sources, 619 MSPs remain and serve as the basis for Pop. I.

To ensure greater precision, the Shklovskii effect [109] and the differential Galactic rotation [110] should be considered in correcting the  $\dot{P}$  (also consequently  $\dot{f}_{\rm rot}$ ). The GW detectability, discussed in the subsequent sections, mostly depends on the high-ellipticity tail of the ellipticity distribution, which scales with  $\dot{P}$  (Eqs. (8) and (13)). However, as demonstrated in Fig. 1 of Ref. [81], such corrections are negligible for rather lager values of  $\dot{P}$ . Therefore, the influence of these effects on GW detectability is insignificant in our work.

From this selected sample, we generate smooth probability density functions (PDFs) for the observable quantities  $f_{\rm rot}$  and  $\dot{f}_{\rm rot}$  using a Kernel Density Estimation (KDE) method [111]. The distribution for the surface magnetic field,  $B_{\rm surf}$ , is then derived following Eq. (7). These three resulting PDFs collectively define the present-day parameter distributions of Pop. I, as presented in Fig. 1.

For our second framework, the Pop. II, we generate present-day parameter distributions from a set of universal birth parameters, following the methodology and best-fit results of Ploeg et al. [59]. Ref. [59] provides the necessary birth-property distributions: a log-normal distribution for the surface magnetic field,  $B_{\text{surf}}$ , and another for the initial rotation period,  $P_i$ . We then evolve these initial periods to their present-day values using the age distribution of the bulge MSPs, which is derived from a convolution of the bulge's ancient star formation rate (SFR) and the Delay Time Distribution (DTD). We note that Ref. [59] models the bulge as two components: a larger, dominant boxy bulge and a smaller nuclear bulge. Their best-fit results indicate that the number of MSPs in the boxy bulge is substantially larger than in the nuclear bulge (by a factor of about 5). Therefore, for our model, we simplify this by considering only the dominant boxy bulge component, using its specific star-formation history to derive the age distribution.

By sampling from the birth distributions of  $P_i$  and  $B_{\rm surf}$  and evolving each MSP over its sampled age, we generate the present-day period (P) distribution for the bulge population. With the distributions for the present-day period P and the (time-independent) magnetic field  $B_{\rm surf}$  established, we then induce the distribution for the period derivative,  $\dot{P}$ , using the same force-free magnetosphere relation as before:

$$\dot{P} = \frac{5\pi^2 R_{\text{MSP}}^6 B_{\text{surf}}^2}{3c^3 I_{zz} P}.$$
 (16)

By simulating a large ensemble, we produce the final evolved distributions for  $f_{\rm rot}$ ,  $\dot{f}_{\rm rot}$ , converted from P and  $\dot{P}$ , and  $B_{\rm surf}$ , presented in Fig. 1. This provides a self-consistent, physically motivated model of the Galactic bulge MSP population.

## B. Ellipticity distribution

Fig. 2 presents the ellipticity distributions of bulge MSPs under the three considered scenarios. These distributions are obtained by combining the parameter distributions from the previous subsection with the ellipticity origins discussed in Sec. III. For the magnetic-field-induced deformation scenario (left panel), Pop. I yields slightly higher ellipticities than Pop. II, reflecting their differing distributions of  $B_{\rm surf}$ ,  $f_{\rm rot}$ , and  $|\dot{f}_{\rm rot}|$  (Fig. 1). For the crustal mountains scenario (middle panel), both populations exhibit the same  $\delta$ -function-like distribution. For the energy-loss-fraction scenario (right panel), the two populations again show nearly identical distributions, as differences in  $f_{\rm rot}$  and  $|\dot{f}_{\rm rot}|$  effectively cancel out in Eq. (14).

### C. Morphology

The morphology of the GCE provides crucial information about its origin. While early analyses suggested a spherically symmetric profile, such as a generalized Navarro-Frenk-White (gNFW) profile consistent with dark matter annihilation, compelling recent evidence indicates that the GCE's spatial distribution may correlate with the stellar mass of the Galactic bulge [45–48]. This finding thus supports an astrophysical origin, such as a population of unresolved MSPs [112].

Given our focus on investigating the GW signal from the MSPs responsible for the GCE, we adopt a morphology that traces the stellar bulge over a gNFW profile. Following the physically motivated model in Refs. [47, 48, 59], we specifically adopt the boxy bulge configuration [113, 114]. We consider another well-motivated bulge model—the spherical bulge in Appendix B, and find that our GW signal predictions are insensitive to the assumed bulge morphology.

This spatial distribution of the boxy bulge model is described by:

$$\rho_{\text{boxy}} \propto \text{sech}^2(R_s) \times \begin{cases} 1 & R \le R_{\text{end}} \\ \exp\left\{-\frac{(R-R_{\text{end}})^2}{h_{\text{end}}^2}\right\} & R > R_{\text{end}}, \end{cases}$$
(17)

where R is the cylindrical Galactocentric radial distance, with  $R_{\rm end}=3128~{\rm pc}$  and  $h_{\rm end}=461~{\rm pc}$ . The quantity  $R_s$  is a scaled radius defined by:

$$R_{\perp}^{C_{\perp}} = \left(\frac{|x'|}{1696 \text{ pc}}\right)^{C_{\perp}} + \left(\frac{|y'|}{642.6 \text{ pc}}\right)^{C_{\perp}}$$
 (18)

$$R_s^{C_{\parallel}} = R_{\perp}^{C_{\parallel}} + \left(\frac{|z'|}{442.5 \text{ pc}}\right)^{C_{\parallel}},$$
 (19)

with power-law indices  $C_{\parallel}=3.501$  and  $C_{\perp}=1.574$ . The primed coordinates (x',y',z') are Cartesian coordinates within the boxy bulge's reference frame. This frame is obtained by rotating the standard Galactocentric frame

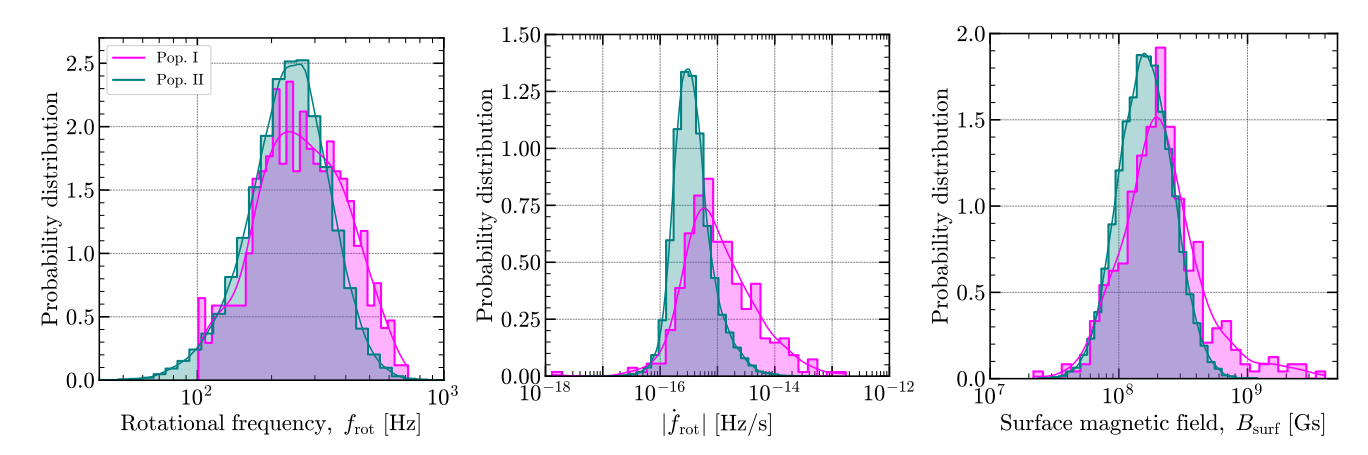


FIG. 1: Distributions of parameters of bulge MSPs responsible for the GCE. Pink: Pop. I derived from the filtered ATNF pulsar catalog [104]. Green: Pop. II derived from Ploeg et al. [59]. Left and Middle: Distributions of the rotational frequency  $f_{\rm rot}$  and its derivative  $\dot{f}_{\rm rot}$ , respectively. Right: Distributions of the surface magnetic field  $B_{\rm surf}$ , computed using Eq. (7). In all panels, the curves represent the KDEs derived from the sample for the corresponding parameters.

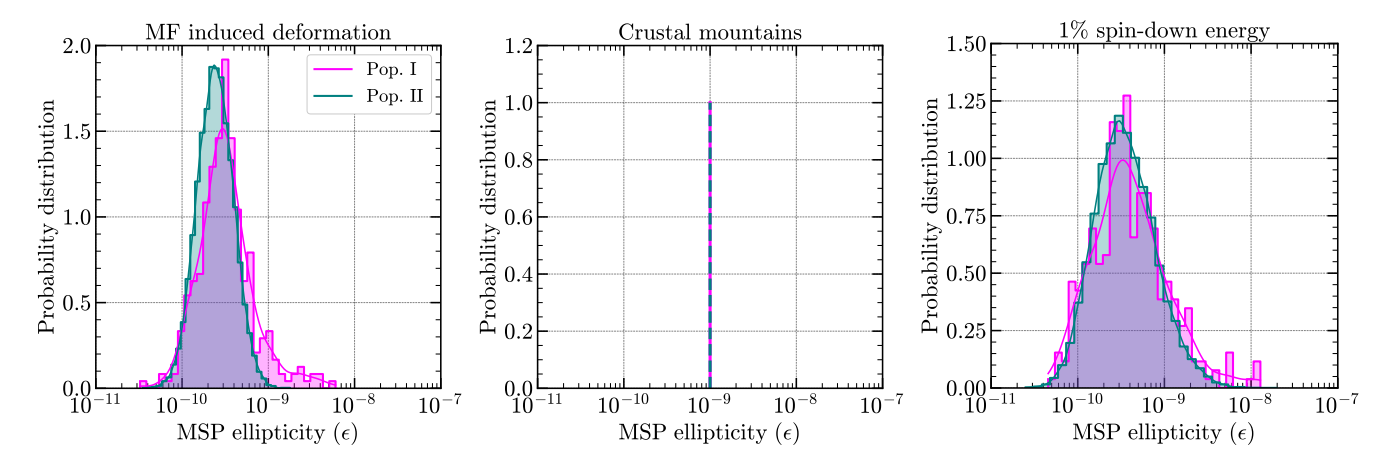


FIG. 2: Distributions of ellipticities of bulge MSPs from three distinct scenarios. Pink: Pop. I derived from the filtered ATNF pulsar catalog [104]. Green: Pop. II derived from Ploeg et al. [59]. Left: Magnetic-field-induced deformation. Middle: Crust mountains from breaking strain. Right: Model independent spin-down energy fraction with  $\eta = 1\%$ . The curves in the left and right panels represent the KDEs derived from the sample for the corresponding parameters.

(in which the Sun is located at  $x_{\odot} = -R_0, y_{\odot} = z_{\odot} = 0$ ) first by 13.79° around the z-axis, and then by 0.023° around the new y'-axis.

#### D. MSPs' total number and luminosity functions

For the Pop. I, the total population size,  $N_{\rm MSP}$ , is a key input parameter that must be benchmarked from existing literature. The comprehensive analysis of Ref. [115] provides an ideal framework for this purpose. Their work tested several benchmark luminosity functions, finding that models based on Globular Cluster (GLC) or Non-Poissonian Template Fitting (NPTF) data are in strong tension with observations, as they overproduce the number of resolved point sources. From the observationally

viable frameworks presented in their analysis, we select the Accretion-Induced Collapse (AIC) [49] benchmark as the basis for our population estimate. This choice is dually motivated: first, the model is fully consistent with the resolved source constraints from the GCE. Second, its prediction, a total population of  $N_{\rm gNFW} \approx 3.6 \times 10^5$  for a gNFW profile [116–118], aligns with independent, recent analyses using machine learning, which show a preference for a large population of  $N_{\rm MSP} > 10^5$  [106].

Since our model adopts the boxy bulge morphology, we must rescale this benchmark number to account for the different spatial geometry while preserving the total GCE flux. The scaling is determined by the ratio of the flux-to-luminosity factors (F/L) for the two profiles. We numerically compute the F/L ratio for both the gNFW

and our boxy bulge profiles using the standard relation:

$$\frac{F}{L} = \frac{1}{4\pi} \frac{\int_{\Omega} d\Omega \int_{0}^{\infty} ds \, \rho(s, \Omega)}{\int_{\Omega} d\Omega \int_{0}^{\infty} s^{2} ds \, \rho(s, \Omega)},\tag{20}$$

where  $\rho$  is the spatial density for the respective profile. The required number of MSPs for our model is then given by the scaling relation:

$$N_{\text{boxy}} = N_{\text{gNFW}} \times \frac{(F/L)_{\text{gNFW}}}{(F/L)_{\text{boxy}}}.$$
 (21)

Our calculation of this geometric factor indicates that for our region of interest (ROI), the boxy bulge profile is slightly more spatially concentrated than the gNFW profile, resulting in a scaling factor of approximately 0.8. Applying this factor to the AIC benchmark number, we obtain our baseline estimate of approximately  $2.9 \times 10^5$  MSPs for the Pop. I.

In contrast to the Pop. I, the total size of the bulge population for the Pop. II is not a free parameter but a derived quantity. It is determined by the normalization required for the model's derived luminosity function to reproduce the total GCE flux. We therefore adopt the total population size as estimated by Ploeg et al. [59], but must rescale it to our specific ROI.

Their analysis, which fits the GCE flux within the region  $|\ell| < 20^{\circ}$  and  $|b| < 20^{\circ}$  (hereafter  $\Omega_{\rm Ploeg}$ ), suggests a total of  $N_{\rm Ploeg} \approx 34000$  MSPs. This number, however, represents the combined population from both the boxy and nuclear bulge components described in their model. Our analysis focuses on the boxy bulge, as our ROI mask ( $|b| > 2^{\circ}$ ) preferentially removes the central Galactic plane where the highly concentrated nuclear bulge resides. We therefore first isolate the number of MSPs belonging to the boxy bulge component. Using the best-fit ratio from Ref. [59],  $\log_{10}(N_{\rm nuclear}/N_{\rm boxy}) \approx -0.66$ , we can get the boxy bulge comprises a fraction  $f_{\rm boxy} \approx 0.82$  of the total population.

Then we should account for the different solid angles of the analysis regions. We calculate the fraction of the boxy bulge population residing within our masked ROI ( $|\ell| < 20^{\circ}$ ,  $2^{\circ} < |b| < 20^{\circ}$ , hereafter  $\Omega_{\rm ROI}$ ) relative to the population within the unmasked region of Ref. [59] This geometric scaling factor,  $f_{\rm ROI}$ , is the ratio of the volume integrals of the density profile over the respective solid angles:

$$f_{\rm ROI} = \frac{\int_{\Omega_{\rm ROI}} d\Omega \int_0^\infty ds \, s^2 \, \rho_{\rm boxy}(s, \Omega)}{\int_{\Omega_{\rm Ploeg}} d\Omega \int_0^\infty ds \, s^2 \, \rho_{\rm boxy}(s, \Omega)}.$$
 (22)

By numerically evaluating this expression, we find that approximately 58% of the boxy bulge MSPs within  $\Omega_{\text{Ploeg}}$  are contained in our ROI. The final population size for our model is therefore the product of these two correction factors applied to the total population range from Ref. [59],  $N_{\text{MSP}} = N_{\text{Ploeg}} \times f_{\text{boxy}} \times f_{\text{ROI}}$ . This yields a baseline estimate of  $N_{\text{MSP}} \approx 16170$  for the Pop. II.

## V. MSP GW DETECTION STRATEGIES: COHERENT VS INCOHERENT

# A. Continuous Monochromatic GW Detection

As shown in Eq. (1), the GW emission from an MSP is monochromatic, at  $f_{\rm GW}=2f_{\rm rot}$ . In this case, the minimum detectable strain amplitude for a continuous monochromatic wave at a given signal-to-noise ratio (SNR) is [80]

$$h_0^{\min} = \frac{\text{SNR}}{\left\langle F_+^2 \right\rangle^{1/2}} \sqrt{\frac{S_n \left( f_{\text{GW}} \right)}{T_{\text{obs}}}} \cdot \frac{1}{\sqrt{4/5}}, \qquad (23)$$

where  $S_n(f_{\rm GW})$  represents the power spectrum density (PSD) of detectors evaluated at frequency  $f_{\rm GW}$ , and  $T_{\rm obs}$  is the effective observation time. For  $\langle F_+^2 \rangle^{1/2}$ , we use the root-mean-square antenna response to the "+" polarization, averaged over source sky position and polarization during one sidereal day, yielding  $\sqrt{1/5}$  for interferometers. The extra factor  $\sqrt{4/5}$  arises from averaging over an isotropic distribution of the inclination angle  $\iota$  between the pulsar rotation axis and the line of sight, as described in Eq. (1). Finally, for our MSPs clustered near the GC rather than isotropically distributed over the full sky, the antenna pattern average differs from the all-sky value by only a few percent [73, 103], which we neglect.

The frequency resolution is given by

$$(\Delta f)^{\rm res} \simeq \frac{1}{T_{\rm obs}} \,.$$
 (24)

The decrease of  $h_0^{\text{min}}$  with  $T_{\text{obs}}$  in Eq. (23) can also be understood as that reducing the bandwidth  $(1/T_{\text{obs}})$  accepts less noise while the monochromatic signal stays the same.

#### B. Complications due to Doppler Shifts

However, the signal at detection at a specific time is shifted in frequency due to Doppler effects, which originate from the Earth's rotation and revolution and possible orbital motion of the MSP if it is in a binary system. In a time period  $T_{\rm obs}$ , the relative velocity of the Earth and the source changes with time, which produces a time-varying Doppler shift in the frequency. In the frequency domain, this manifests as a Doppler broadening/smearing, with the width set by the maximum Doppler shift with  $T_{\rm obs}$ , denoted by  $(\Delta f)^{\rm max}$ . Once the  $(\Delta f)^{\rm max}$  becomes comparable to the frequency resolution  $1/T_{\rm obs}$ , increasing  $T_{\rm obs}$  further does not improve substantially the SNR, as it reduces both accepted noise and signal, and Eq. (23) is no longer applicable.

We estimate the maximum Doppler shifts,  $(\Delta f)^{\text{max}}$ , as follows. First, considering the Earth's rotation, at latitude 40° (approximately match the location of the current and future ground-based GW detectors), the surface

velocity is  $v_{\rm rot} = \omega_{\rm rot} R_{\oplus} \cos{(40^{\circ})} \simeq 355 \,\mathrm{m/s}$ , where  $\omega_{\rm rot} = 2\pi/(24\,\mathrm{hr})$  and  $R_{\oplus}$  is the Earth's radius. This leads to a maximum frequency shift when the detector reverses its velocity relative to the MSP (every  $\simeq 12$  hours) [80],

$$(\Delta f)_{\text{rot}}^{\text{max}} \simeq 2f_0 \frac{v_{\text{rot}}}{c} \simeq 4.8 \times 10^{-3} \text{ Hz} \left(\frac{f_0}{2 \text{ kHz}}\right).$$
 (25)

Second, for Earth's revolution (approximated as circular with  $v_{\rm orb} \simeq 3 \times 10^4 \,\mathrm{m/s}$ ), the maximum Doppler shift is (every  $\simeq 6$  months) [80]

$$(\Delta f)_{\text{orb}}^{\text{max}} \simeq 2f_0 \frac{v_{\text{orb}}}{c} \simeq 0.4 \text{ Hz} \left(\frac{f_0}{2 \text{ kHz}}\right).$$
 (26)

Finally, for the orbital motion of the MSPs in the binary systems, the maximum Doppler shift (every half orbital period), as estimated from the ATNF pulsar catalog samples [104], is found to be

$$(\Delta f)_{\rm bin}^{\rm max} \simeq 2f_0 \frac{v_{\rm bin}}{c} \simeq 2.0 \text{ Hz} \left(\frac{f_0}{2 \text{ kHz}}\right),$$
 (27)

with further details provided in Appendix A.

Therefore, as long as  $T_{\rm obs}$  is longer than  $\sim 1$  hour, the Doppler shifts are important and Eq. (23) is no longer applicable.

Doppler shift can, in principle, be corrected by defining a new time variable  $t' = t + (\mathbf{x}(t) \cdot \hat{\mathbf{r}})/c$  [80], where  $\mathbf{x}(t)$  is the position of the detector and  $\hat{\mathbf{r}}$  is the unit vector pointing toward the source. However, to correct the Doppler shift, the location of the MSPs needs to be known accurately, e.g.,

$$\Delta \theta < 0.1 \operatorname{arcsec} \left(\frac{10^7 \,\mathrm{s}}{T}\right)^2 \left(\frac{1 \,\mathrm{kHz}}{f_0}\right) \,.$$
 (28)

For bulge MSPs, their locations are unknown, but one can, in principle, perform blind searches over the GCE region with the pixel size smaller than that set by Eq. (28). However, this would cost a huge amount of computational power, which scales at least as  $\sim T_{\rm obs}^5$ . Even though the Doppler shifts due to the Earth's motion can be corrected by redefining the time variable, the orbital motion of bulge MSPs in binary systems is unknown; since most MSPs are expected to be in binaries, such Doppler modulation cannot be corrected in the same way.

# C. Our Approach: Two Detection strategies

Motivated by the discussion above, we consider two strategies for detecting bulge MSPs.

The first is the coherent strategy, which assumes that all Doppler shifts can be corrected. This is feasible for isolated MSPs in blind searches with sufficiently small pixel sizes (Eq. (28)), provided that adequate computational power is available. In this case, an individual MSP

becomes detectable once its GW strain amplitude  $(h_0; \text{Eq. (2)})$  exceeds the sensitivity threshold  $(h_0^{\min}; \text{Eq. (23)})$  with SNR = 5 [79, 119] and  $S_n$  for different detectors, i.e.,

$$h_0 > h_0^{\min}$$
. (29)

The second is the incoherent strategy, which assumes that the MSP's Doppler shifts cannot be fully corrected, either due to limited computational power in blind searches or because of unknown orbital modulation in binary systems. In this case, the signal from an individual MSP is no longer confined to a single Fourier bin  $((\Delta f)^{\rm res} \sim 1/T_{\rm obs})$ , but broadened to a width  $(\Delta f)^{\rm max} \gg 1/T_{\rm obs}$  set by the maximum Doppler shift within  $T_{\rm obs}$ . As a consequence, a fully coherent integration over the entire  $T_{\rm obs}$  is not possible.

A standard approach is to divide the data into N shorter coherent segments of duration  $T_{\rm stack}$ , such that  $1/T_{\rm stack} \sim (\Delta f)^{\rm max}$  holds within each segment. Each stack is analyzed coherently, and then the results are combined incoherently across  $N = T_{\rm obs}/T_{\rm stack}$  segments. The corresponding sensitivity for incoherent search is degraded compared to the coherent case by a factor of  $N^{1/4}$  [80]:

$$h_0^{\text{min,incoh}} = \frac{\text{SNR}}{\langle F_+^2 \rangle^{1/2}} \sqrt{\frac{S_n(f_0)}{T_{\text{obs}}}} \cdot \frac{1}{\sqrt{4/5}} \cdot \left(\frac{T_{\text{obs}}}{T_{\text{stack}}}\right)^{\frac{1}{4}},$$
(30)

where  $(T_{\rm obs}/T_{\rm stack})^{1/4}$  quantifies the loss of sensitivity due to loss of phase coherence across the broadened bandwidth. Motivated by discussions in Sec. VB, we choose  $1/T_{\rm stack} = (\Delta f)^{\rm max} = 2$  Hz. In the frequency domain, this is equivalent to binning the signals of the MSPs into different frequency window.

For  $\langle F_+^2 \rangle$  in Eq. (30), we adopt the standard sky-, polarization-, and inclination-averaged value of 1/5, consistent with Eq. (23). Strictly speaking, such an average is valid when the observation time is long compared to a sidereal day, so that the apparent motion of the sources averages over right ascension and polarization. In our case, although each coherent segment is only  $T_{\rm stack} = 0.5$  s, the total observation time can exceed a year. Moreover, the signal is an incoherent sum over  $\mathcal{O}(10^5)$  MSPs near the GC (discussion below), whose orientations  $(\iota, \psi)$  can be regarded as effectively random. These two facts justify the use of the averaged antenna pattern in Eq. (30), and deviations from the exact instantaneous values are expected to be negligible in our setup.

Since the phase information is lost between different stacks, the incoherent strategy is sensitive only to the summed power of the signals within the frequency window  $(\Delta f)^{\max}$ . In practice, the effective strain amplitude from multiple MSPs that fall into the same frequency window can be written as

$$h_{\text{eff}} = \left(\frac{\pi}{4} \sum_{i \in (\Delta f)^{\text{max}}} h_{0,i}^2\right)^{1/2},$$
 (31)

where  $h_{0,i}$  is the intrinsic strain amplitude of the *i*-th MSP and the factor  $\pi/4$  originates from the random selection of phase angles. Detection occurs when

$$h_{\text{eff}} > h_0^{\text{min,incoh}}.$$
 (32)

Therefore, in the incoherent strategy, the observables are no longer individual monochromatic signals, but rather, the collective excess power within each Doppler broadened frequency window.

Between the (fully) coherent and (fully) incoherent strategies discussed above, many continuous GW search pipelines employ a semicoherent approach [103, 108, 120]. This allows exploring a large parameter space at a reasonable computational cost, with only a relatively small sensitivity loss compared to the coherent strategy. In this case, the data are divided into segments that are moderately longer than  $T_{\rm stack} = 0.5$  s used in our incoherent strategy, so that more phase information is preserved. Each segment is analyzed coherently, and the results are then combined incoherently. As a result, the sensitivity and detectability of semicoherent searches fall between the coherent and incoherent strategies considered above. We do not consider this case separately in our forecasts. since its performance can be conservatively bracketed by the coherent and incoherent strategies.

#### VI. RESULTS AND DISCUSSION

Fig. 3 shows our results on the intrinsic strain amplitudes of the bulge MSPs responsible for the GCE, for different ellipticity origins (Sec. III) and MSP population models (Sec. IV A), along with the sensitivity of continuous GW searches from current and future ground-based GW detectors. The results in the left column, from our Pop. I MSP population model based on the ATNF pulsar catalog [104], are generally higher than those in the right column, from our Pop. II model based on Ploeg et al. [59], mainly because the former has a  $N_{\rm MSP}$  about 10 times larger. In addition, the distributions in  $f_{\rm GW}=2f_{\rm rot}$  and ellipticity in the two population models also lead to a difference in the strain amplitude.

The relative placement of the scattered points with respect to the **solid** sensitivity curves [121] illustrates the prospects of detecting those individual MSPs in the coherent strategy, while in the incoherent strategy, detectability is assessed by comparing the green dashed line with the **dashed** sensitivity curves. Overall, for the **coherent strategy**, the predicted  $h_0$  values are below the reach of current detectors [67–69] but can be detectable by next-generation detectors like CE and ET [70, 71]. For the **incoherent strategy**, only the theoretical maximum from Pop. I marginally exceeds the sensitivity of CE with a one-year observation time.

The scatter of the points is mainly due to the broadness of the ellipticity distribution (Fig. 2), the Earth-MSP distance distribution from the morphological model (Fig. 5), and the frequency distribution (Fig. 1). This

explains why the crustal mountains scenario (second row of Fig. 3) exhibits the least scatter, since its ellipticity distribution is effectively a delta function.

It is worth noting that the true detectability can be more optimistic than that indicated by our baseline results, as the amplitudes are primarily controlled by (1) the total number of MSPs,  $N_{\rm MSP}$ , and (2) the physical quantities affecting MSP ellipticity in each scenario. For the former, the  $h_0$  values of individual MSPs are primarily influenced by  $N_{\rm MSP}$  through the spread of their distribution, such that a larger  $N_{\rm MSP}$  results in more MSPs populating the high- $h_0$  tail. In contrast, the effective summed strain  $h_{\rm eff}$  scales directly with  $N_{\rm MSP}$ . Thus, while a larger  $N_{\rm MSP}$  enhances detectability in both the coherent and incoherent strategies, it does so through different mechanisms. For the latter, we discuss each scenario separately in the following text.

The top row of Fig. 3 shows the case in which ellipticity is sourced by strong internal magnetic fields misaligned with the rotation axis. All MSPs fall below the sensitivity of current detectors, but the most extreme sources in the high- $h_0$  tail are detectable with CE or ET for the Pop. I. Besides the influence of  $N_{\rm MSP}$  discussed above, the overall normalization of  $h_0$  and  $h_{\rm eff}$  is proportional to  $B_{\rm int}$ , for which we adopt a conservative benchmark of  $150B_{\rm surf}$  for a direct comparison with previous work (e.g., Refs. [73, 74]). A higher value of  $B_{\rm int}$  will enhance detectability, as  $B_{\rm int}/B_{\rm surf}$  for MSPs is expected to be  $10^2-10^4$  [91–93].

The second row of Fig. 3 corresponds to the scenario in which the ellipticity is sustained by crustal deformations at the long-term residual level. We adopt a representative ellipticity of  $10^{-9}$ , which sets the overall normalization of both  $h_0$  and  $h_{\rm eff}$ , which are also influenced by  $N_{\rm MSP}$  discussed above. Because the ellipticity is fixed, the differences between the two population models arise solely from  $N_{\rm MSP}$  and the distribution of  $f_{\rm GW}$ . The resulting  $h_0$  values are generally smaller than those in the magnetic-field scenario, and their detectability is correspondingly more difficult, remaining beyond the sensitivity of current and next-generation detectors.

The third row of Fig. 3 shows results when a fraction  $\eta$  of the spin-down energy is assumed to be emitted as GWs. We take  $\eta=1\%$  as a benchmark. Note that  $\sqrt{\eta}$  sets the overall normalization of both  $h_0$  and  $h_{\rm eff}$ ; both are additionally shaped by the influence of  $N_{\rm MSP}$  discussed above. In this scenario, the MSPs in the high- $h_0$  tail can exceed the sensitivity of ET or CE.

Finally, the bottom row of Fig. 3 shows the theoretical maximum case, where  $\eta=100\%$ , i.e., all spin-down energy is converted into GW emission. In this maximum scenario, both  $h_0$  and  $h_{\rm eff}$  are a factor of 10 larger than in the  $\eta=1\%$  case in the third row, representing the absolute upper bound on the GW emission from MSPs. Remarkably, LVK O4 can observe a fraction of the MSPs in the high- $h_0$  tail, implying that Advanced LIGO and Virgo at design sensitivity can potentially detect some individual sources [78, 79]. Conversely, a null

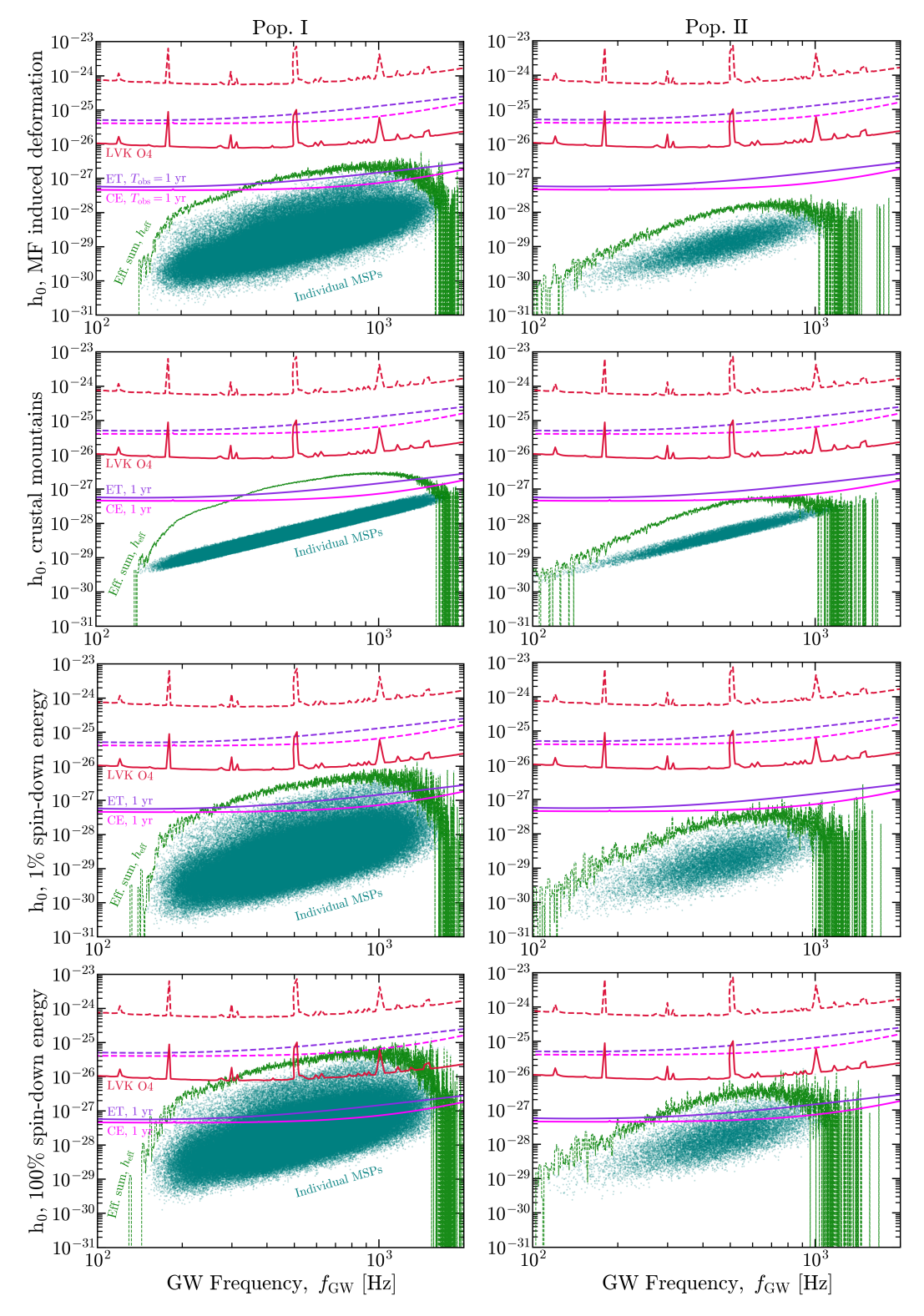


FIG. 3: (Main results of the paper.) Our results for the intrinsic strain amplitude  $h_0(f_{\rm GW})$  of bulge MSPs responsible for the GCE, shown for different ellipticity origins (vertical panels; Sec. III) and MSP population models (horizontal panels; Sec. IV A), along with the sensitivity for continuous wave searches from different GW detectors, as labeled. The **scattered points** represent our predicted  $h_0$  for the individual MSPs, to be compared with the **solid** sensitivity curves (coherent strategy; Eq. (23)). The **green dashed lines** represent the total effective strain amplitude (Eq. (31)) from the MSPs within a 2-Hz bin, to be compared with the **dashed** sensitivity lines (incoherent strategy; Eq. (30)). **Top row**: ellipticity originating from magnetic-field-induced deformation (Sec. III A). **Second row**: ellipticity originating from crustal mountains from breaking strain (Sec. III B). **Third row**: ellipticity assuming  $\eta = 1\%$  of spin-down energy converts to GW emission (Sec. III C). **Bottom row**: theoretical maximum, assuming  $\eta = 100\%$  of spin-down energy converts to GW emission (Sec. III C). **Left column:** MSP Population I based on the ATNF pulsar catalog [104]. **Right column:** MSP Population II based on Ploeg et al. [59].

detection in O4 can place meaningful constraints on such optimistic scenarios, carrying important implications for the maximum possible ellipticities of MSPs and their role in explaining the GCE.

Our results are all based on the boxy bulge model. Appendix B, we show that they are insensitive to the assumed bulge morphology.

Moreover, our results are based on the ROI of  $|\ell| < 20^\circ$  and  $2^\circ < |b| < 20^\circ$ . However, there are likely many MSPs within  $|\ell| < 20^\circ$  and  $|b| < 2^\circ$ . This Galactic plane region causes significant contamination in gamma-ray observations, but this may not be the case for GW observations. In Appendix C, we show that including this region increases the total number of MSPs by 70%, thereby leading to only a modest increase in the GW signal and its detectability.

### A. Compare with previous work

Our detectability is a few orders of magnitude lower compared with Ref. [73] by Miller & Zhao. The main reason is that Ref. [73] included PSR J0537-6910 in their ATNF-catalog-drive MSP population model, which dramatically boosted their detectability estimate.

PSR J0537-6910 has quite different properties from MSPs. Although its period is 16.2 ms, only slightly larger than that of typical MSPs (1–10 ms), its period derivative is  $\dot{P} = 5.2 \times 10^{-14}$ , many orders of magnitude larger than those of typical MSPs  $(10^{-21}-10^{-19})$ . As a result, the spin-down power is  $\dot{E} \simeq 5 \times 10^{38}$  erg/s, enormously higher than typical MSPs  $(10^{33}-10^{35} \text{ erg/s})$ . The corresponding spin-down age is only  $\simeq 4.9 \times 10^3$  yr, and the derived surface magnetic strength is  $\simeq 9.3 \times 10^{11}$  Gs, both consistent with a young pulsar rather than an MSP ( $\sim 1 \text{ Gyr and } \sim 10^8 \text{--}10^9 \text{ Gs}$ ). Thus, Ref. [73] derived an ellipticity of  $\simeq 10^{-6}$  for PSR J0537-6910, which is a strong outlier in their ellipticity distribution (see their Figs. 4 and 5), and this drives their detectability by orders of magnitude. We do not include PSR J0537-6910 because its above properties indicate that it is a young pulsar rather than an MSP. Moreover, PSR J0537-6910 is located in the Large Magellanic Cloud (LMC) rather than in the Milky Way [122].

One might ask whether a population of young pulsars similar to PSR J0537-6910 could reside in the bulge region ( $|\ell| < 20^{\circ}$  and  $2^{\circ} < |b| < 20^{\circ}$ ) and thereby account for the GCE. Our estimate indicates that the expected number of such objects is  $\ll 1$ , as follows. Nearly all the young pulsars originate from Galactic core-collapse supernovae (SNe), occurring at a rate of  $\simeq 0.02 \text{ yr}^{-1}$ . For  $|\ell| < 20^{\circ}$  (corresponding to Galactocentric radius < 3 kpc), the fraction of pulsar density is  $\sim 0.1$ , obtained by integrating a normalized standard pulsar birth surface density profile, modeled as a shifted Gamma function [123, 124], up to 3 kpc. For  $|b| > 2^{\circ}$  (i.e., Galactocentric height z > 0.3 kpc), the fraction is  $\sim 0.4$ , derived by integrating an exponen-

tial vertical distribution (normalized)  $\propto e^{-|z|/H}$  with the young pulsars' scale height of  $H=330~{\rm pc}$  [124]. Among the several thousand pulsars listed in the ATNF pulsar catalog [104], PSR J0537-6910 has the highest spindown power and is the only young pulsar with a rotational frequency comparable to MSPs. Thus, the fraction  $(f_{\rm fast})$  of such extreme young pulsars is very small, i.e.,  $f_{\rm fast} \sim \mathcal{O}(1/N_{\rm pulsar}) \ll 1$  as an order-of-magnitude estimate, where  $N_{\rm pulsar}$  is the total number of cataloged pulsars. Combining the above factors and adopting a time window of 5 kyr (the age of PSR J0537-6910), the expected number of comparable young pulsars in the bulge region is  $\sim 5~{\rm kyr} \times 0.02~{\rm yr}^{-1} \times 0.1 \times 0.4 \times f_{\rm fast} = 4f_{\rm fast} \ll 1$ .

As a comparison to the above, including one such object in the bulge MSP population models would imply the existence of  $\sim 500$  analogous young pulsars in Pop. I and  $\sim 30$  in Pop. II, obtained by scaling the total predicted MSP numbers (Sec. IV D) by the sample size of 619 MSPs in our ATNF-based empirical population model. These values exceed the above estimate,  $4f_{\rm fast}$ , by orders of magnitude. Furthermore, Ref. [106] showed that even if the GCE is due to point sources, the total number of MSPs should be  $\sim 10^5$ , much larger than any plausible young-pulsar population.

In addition, a pulsar with its immense spin-down power, of which J0537-6910 exhibits the maximum among detected pulsars, would generate conspicuous observational signatures, such as a bright pulsar wind nebula (PWN). Indeed, the PWN powered by PSR J0537-6910 is so prominent that it has been detected by both Fermi-LAT [125] and H.E.S.S. [126], despite its location outside our galaxy in the LMC. While these are indirect, such prominent features would increase the probability of identifying this kind of object. Despite this, no other candidate with comparable properties has been observed, which strongly implies the intrinsic rarity of such pulsars. This further illustrates that including PSR J0537-6910 is inconsistent with a realistic bulge population model.

In the energy-loss-fraction scenario, our detectability is higher than that in Ref. [73] after removing PSR J0537-6910, this is because Ref. [73] used  $\eta$  instead of  $\sqrt{\eta}$  in Eq. (13) [127].

Next, compared with Ref. [74] by Bartel & Profumo, our detectability in the coherent strategy is much better. The main reason is that the sensitivity curve used in Ref. [74] appears to be taken directly from the detector PSD, whereas in our calculation, we use Eq. (23), which incorporates the exposure time for continuous GWs.

Another important difference lies in the effective strain from multiple MSPs. In Ref. [74], the effective strain  $h_{\text{eff}}$  seems to be evaluated as a linear sum of the individual contributions,  $h_0^{(1)} + h_0^{(2)} + h_0^{(3)} + \cdots$ , which significantly overestimates the collective strain amplitude, whereas we use a quadrature sum given in Eq. (31).

Furthermore, while Ref. [74] adopts the  $B_{\text{surf}}$  distribution from Ploeg et al. [59] (used in our Pop. II), it takes

the P distribution from the ATNF pulsar catalog [104] (used in our Pop. I) instead of that from Ref. [59]. In contrast, our Pop. II adopts all the parameter distributions from Ref. [59] consistently.

#### VII. CONCLUSION

The GCE has long been considered a leading candidate signal for particle dark matter annihilation. However, an unresolved population of MSPs in the Galactic bulge offers the other compelling astrophysical explanation. Distinguishing between these two interpretations is challenging in electromagnetic observations due to source confusion, pulse broadening, and extinction. Gravitational waves, by contrast, provide a dust- and confusion-free probe: a steadily rotating, non-axisymmetric MSP emits a nearly monochromatic GW at about twice its rotational frequency, within the sensitive band of ground-based GW detectors, with amplitude mainly determined by its ellipticity.

In this work, we systematically assess the GW emission expected from a population of MSPs associated with the GCE and evaluate its detectability with current and future GW detectors. To this end, we consider three major scenarios for the origin of MSPs' ellipticity: (1) magnetic-field-induced deformation, (2) longlived crustal mountains from breaking strain, and (3) a model-independent parameterization with a fraction  $\eta$  of the spin-down power emerges as GWs, for which we use  $\eta = 1\%$  as the benchmark and set a theoretical maximum at  $\eta = 100\%$ , i.e., the spin-down limit.

For the population, we constructed (1) an Empirical Disk-Proxy Model (Pop. I) based on MSPs in the ATNF pulsar catalog [104], and (2) an Evolutionary Model (Pop. II) following Ploeg et al. [59], in which bulge MSP properties are evolved from universal birth distributions. We adopted a bulge-tracing boxy bulge morphology and normalized the total numbers to the GCE luminosity, yielding baseline populations of  $N_{\rm MSP} \simeq 2.9 \times 10^5$  (Pop. I) and  $\simeq 1.62 \times 10^4$  (Pop. II) within our ROI after geometric rescaling.

We evaluate the detectability of the GW emission from those MSPs under two search strategies that bracket realistic analyses. In the coherent strategy, we assume the Doppler modulations due to Earth rotation and revolution are correctable (with requires significant computational power) and most MSPs are isolated (i.e., no unknown Doppler modulations due to the binary motion), thus a single Fourier bin collects the signal and the sensitivity follows the standard  $h_{0,\rm min} \propto (1/T_{\rm obs})^{1/2}$  (Eq. (23)). In the incoherent strategy, uncorrected or unknown Doppler modulation broadens the signal power over a frequency window set by the maximal Doppler shift, motivating "stack-slide" strategies with a sensitivity penalty  $\propto (T_{\rm obs}/T_{\rm stack})^{1/4}$  (Eq. (30)) and an effective summed strain  $h_{\rm eff}$  from all MSPs falling in the same frequency window (Eq. (31)).

Our main result, on the GW strain amplitudes and their detectability, is shown in Fig. 3. Overall, in the coherent strategy, the predicted strain amplitudes,  $h_0$ , lie below the reach of current LVK sensitivities, but can be detectable by next-generation detectors such as CE and ET. In contrast, in the incoherent strategy, only the theoretical maximum from Pop. I marginally exceeds the sensitivity of CE. In addition, it is worth noting that the true detectability can be more optimistic than suggested by our baseline forecasts, since the strain amplitudes are primarily governed by two factors: (1) the total number of bulge MSPs,  $N_{\rm MSP}$ , which controls the extent of the high- $h_0$  tail and the summed  $h_{\text{eff}}$ 's normalization, and (2) the physical mechanisms that determine the ellipticity in each origin, which we adopt conservative assumptions. Finally, in the theoretical maximum case with  $\eta = 100\%$ , where all spin-down energy is converted into GW emission, the LVK O4 can potentially detect a fraction of MSPs. Conversely, a null detection in LVK O4 can constrain such optimistic scenarios, with important implications for the maximum sustainable ellipticities of MSPs and their viability in explaining the GCE.

Compared to previous work [73, 74], we conduct a systematic study of the bulge MSPs in the frequency range of ground-based GW detectors. For example, (1) We consider major scenarios in which the MSP ellipticity originates; (2) We outline both coherent and incoherent searching strategies while taking into account the Doppler effects; (3) We consider both isolated MSPs and those in the binary systems. Our detailed analysis yields detectability estimates for the bulge MSPs that are significantly more optimistic than those of Ref. [74], but substantially less optimistic than those of Ref. [73]; see Sec. VI A for details.

Our work also outlines a clear path forward. Directed continuous GW searches toward the GC, optimized for the MSPs' GW frequencies and leveraging various detection methods to manage computational cost, will keep improving current limits. Theoretical and observational inputs are also needed for the MSPs' intrinsic and population properties, especially their ellipticity.

In summary, GW observations offer a unique and complementary window into the Galactic bulge MSP population, overcoming the severe challenges faced in electromagnetic searches. This provides a crucial way to test the MSP interpretation of the GCE, which is the alternative (astrophysical) explanation to the particle dark matter interpretation. Looking ahead, the next generation of GW interferometers will either reveal a long-sought MSP population near the Galactic center or place stringent limits on their ellipticities and abundance. Either outcome will carry profound implications for the origin of the GCE, the role of recycled neutron stars in shaping Galactic high-energy phenomena, and the broader quest to disentangle conventional astrophysical sources from potential dark-matter and other new-fundamentalphysics signatures.

# ACKNOWLEDGMENTS

We are grateful for helpful discussions with Kayla Bartel, John Beacom, Emanuele Berti, Marc Kamionkowski, Gordan Krnjaic, Andrew Miller, Benjamin Owen, Luca Reali, Yue Zhao, and Haowen Zhong. B. Z. is supported by Fermi Forward Discovery Group, LLC under Con-

tract No. 89243024CSC000002 with the U.S. Department of Energy, Office of Science, Office of High Energy Physics. X.H. is supported by the National Key Research and Development Program of China (2022YFF0503304), the National Natural Science Foundation of China (No. 12322302), and the Project for Young Scientists in Basic Research of Chinese Academy of Sciences (No. YSBR-061).

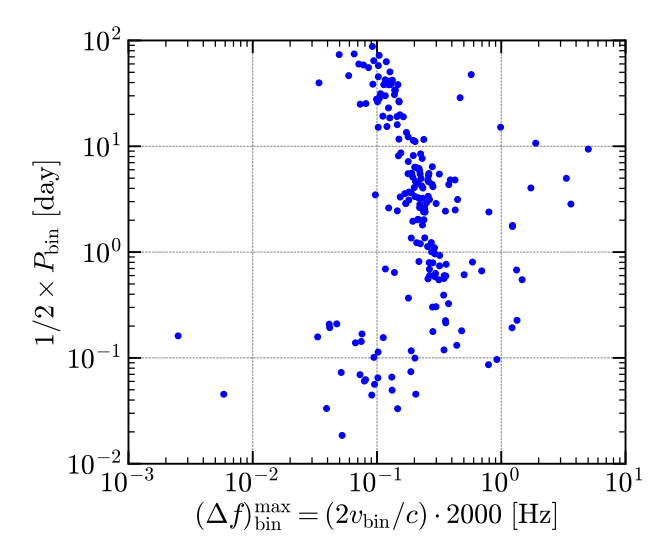


FIG. 4: Distribution of maximum Doppler shifts,  $(\Delta f)_{\rm bin}^{\rm max}$ , versus half orbital period for the 199 MSPs in the binary systems from the ATNF pulsar catalog [104]. Among the 619 MSPs used in the main text, 289 are confirmed to be in binary systems, of which 199 have measured orbital semi-major axis  $a_p$ , orbital period  $P_{\rm bin}$ , and eccentricity e, as required in Eq. (A1).

# Appendix A: Doppler Shifts due to Binary Motion

In Sec. VB, we discuss the Doppler shift in the GW frequency due to Earth's rotation, Earth's revolution, and orbital motion in binary systems. While the first two contributions are well understood, the binary orbital motion varies significantly across binary systems, leading to substantial differences in the maximum Doppler shift.

We determine a maximum Doppler shift in frequency, which applies to most of the MSPs in the binary systems from the ATNF pulsar catalog, by calculating the  $(\Delta f)_{\text{bin}}^{\text{max}}$  for all the confirmed MSPs in binaries. Following the analyses in Refs. [128–130], the orbital velocity of an MSP in the binary system is given by,

$$v_{\rm bin} = \frac{2\pi a_p}{P_{\rm bin}(1-e)},\tag{A1}$$

where  $a_p$  is the orbital semi-major axis,  $P_{\text{bin}}$  is the binary orbital period, and e the orbital eccentricity. Accordingly, the maximum Doppler shift is

$$(\Delta f)_{\rm bin}^{\rm max} \simeq 2 \frac{v_{\rm bin}}{c} f_0,$$
 (A2)

which occurs once every half orbital period.

Fig. 4 shows the distribution of the maximum Doppler shift versus half orbital period for the 199 MSPs in binaries from the ATNF pulsar catalog [104]. The majority of systems exhibit maximum Doppler shifts below 2 Hz, with the distribution peaking around 0.4 Hz, consistent with Eq. (27). A small number of outliers exceed 2 Hz, these generally correspond to systems with high orbital eccentricity e.

# Appendix B: GW Signals Insensitive to Assumed Bulge Morphological Models

In this section, we compare the GW results between different morphological distributions of the MSPs, which primarily affect the distances between the Earth and individual MSPs, which affects the GW strain,  $h_0$  (Eq. (2)). Our conclusion is that our GW results are nearly independent of the assumed morphological models of the bulge.

In the main text, we use the boxy bulge model only. Here, we adopt the other well-motivated model, the spherical bulge model. The spherical bulge follows the density profile [74, 131, 132]:

$$\rho_{\rm sph} \propto \frac{\exp\left(-a^2/a_m^2\right)}{(1+a/a_0)^{1.8}},$$
(B1)

where  $a_m = 1.9$  kpc is the scale length,  $a_0 = 0.1$  kpc is the inner truncation length, and  $a \equiv (x^2 + y^2/\eta^2 + z^2/\zeta^2)$  [131]. Here, (x, y, z) are Cartesian coordinates centered on the GC, and the axis ratios of the bulge are given by:  $1 : \eta : \zeta = 1 : 0.68 : 0.31$  [132].

Fig. 5 presents the two morphological distributions of the galactic bulge: boxy (left panel) and spherical (right panel). The total number of MSPs is based on our Pop. I discussed in the main text.

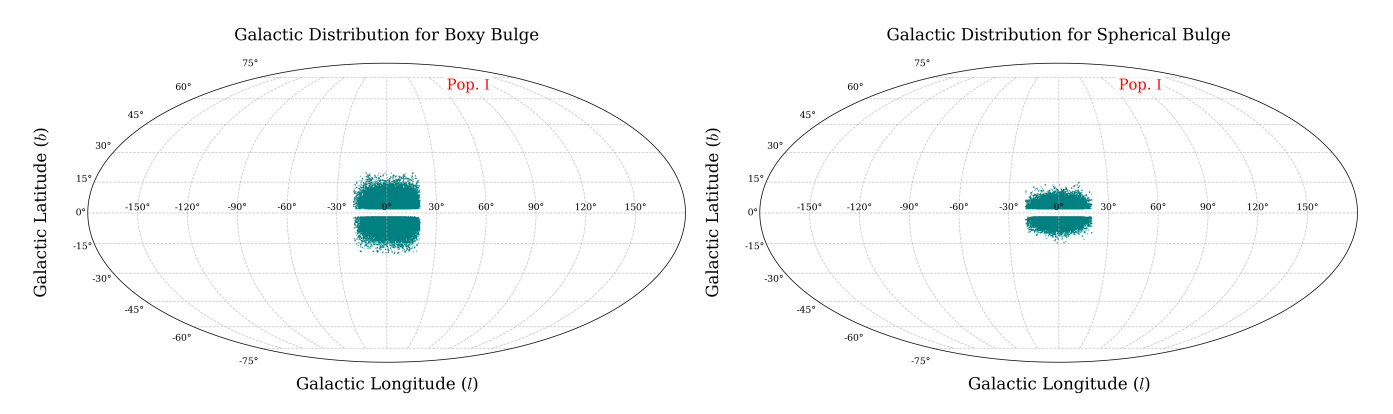


FIG. 5: The distribution of MSPs based on the boxy bulge model (**left**; used in the main text) and the spherical bulge model (**right**).

Fig. 6 compares our GW results among different morphological distributions, including the boxy bulge (left panel) and the spherical bulge (middle panel) discussed above, plus an unrealistic extreme situation, i.e., all the MSPs are placed at the GC. Here, we show the scenario of magnetic-field-induced deformation. Importantly, basically no difference is observed among the three morphological distributions. There are two main reasons. First, the one-dimensional distributions of Earth-MSP distances are more similar between the boxy and spherical morphologies than their corresponding two-dimensional spatial distributions. Second, the ellipticity distribution (Fig. 2, left panel) is much broader than the distance distribution. For the energy-loss-fraction scenario, the same conclusion holds, since both reasons apply. For the crustal mountains scenario, only the first reason applies, because the ellipticity distribution is a delta function (Fig. 2, middle panel); still, the boxy and spherical bulges yield the same results.

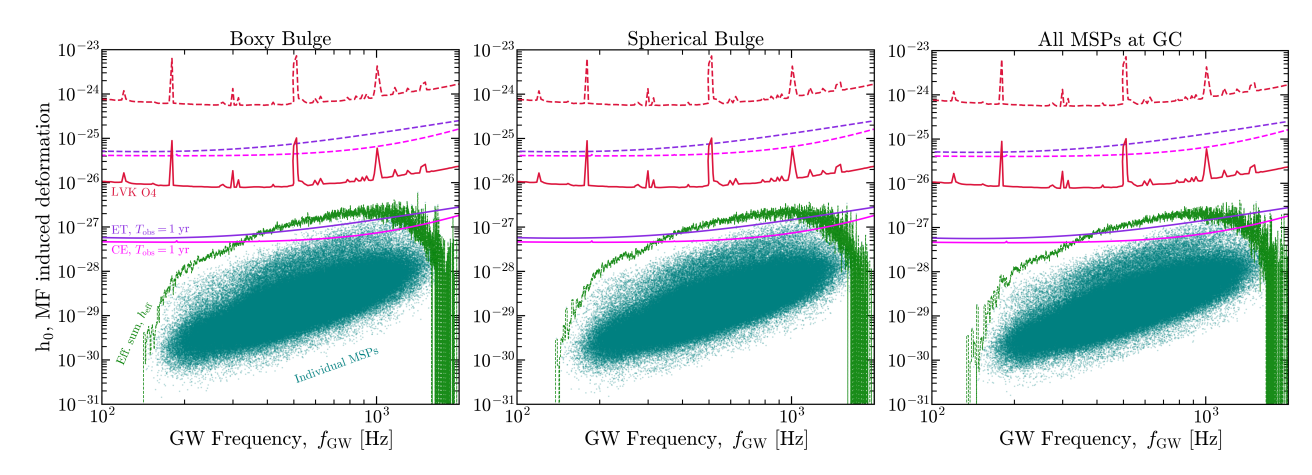


FIG. 6: Similar to Fig. 3 (main results of the paper) but comparing GW signals from the bulge MSPs between three different morphologies: **left:** boxy bulge, used in the main text and identical to the top-left panel of Fig. 3 (but plotted with a different figure size); **middle:** spherical bulge; **right:** all MSPs placed at the GC. Here, we show the ellipticity origin of magnetic-field-induced deformation, for simplicity, and the same conclusion applies to the energy-loss-fraction scenario. For the crustal mountains scenario, the (unrealistic) all-MSPs-at-GC situation is different, but the boxy and spherical morphologies still give the same result. See text for details.

# Appendix C: Results After Including the Galactic Plane

In our main text, we focus on the ROI of  $\Omega_{ROI}$  with  $|\ell| < 20^{\circ}$ ,  $2^{\circ} < |b| < 20^{\circ}$ , in which the Galactic plane is masked. This is consistent with most GCE studies, as the Galactic plane introduces significant contamination in gamma-ray observations. However, this may not be the case for GW observations. Even in gamma-ray observations, some analyses of the GCE retain the Galactic plane [59, 114].

Including the MSPs within  $|b| < 2^{\circ}$  increases the total number of MSPs,  $N_{\rm MSP}$ , thereby enhancing their detectability. We calculate the total number of MSPs with  $|b| < 2^{\circ}$  by scaling the  $N_{\rm MSP}$  within  $|\ell| < 20^{\circ}$  and  $2^{\circ} < |b| < 20^{\circ}$ , derived in Sec. IV D, according to the boxy bulge morphology. The resulting  $N_{\rm MSP}$  within  $|\ell| < 20^{\circ}$  and  $|b| < 20^{\circ}$  is  $5 \times 10^5$  for the Pop. I and 27880 for the Pop. II, about 70% larger than the value obtained when masking  $|b| < 2^{\circ}$  in the main text.

Fig. 7 shows the GW results without masking  $|b| < 2^{\circ}$ . Comparing with the main text results (Fig. 3), we find that although  $N_{\text{MSP}}$  increases by 70%, the improvement in GW detectability remains modest. This is because, for the coherent detection strategy, the increase in detectability arises from populating the high- $h_0$  tails of the distribution, and for the incoherent detection strategy, the enhancement is only  $\sqrt{1.7} \simeq 1.3$ .

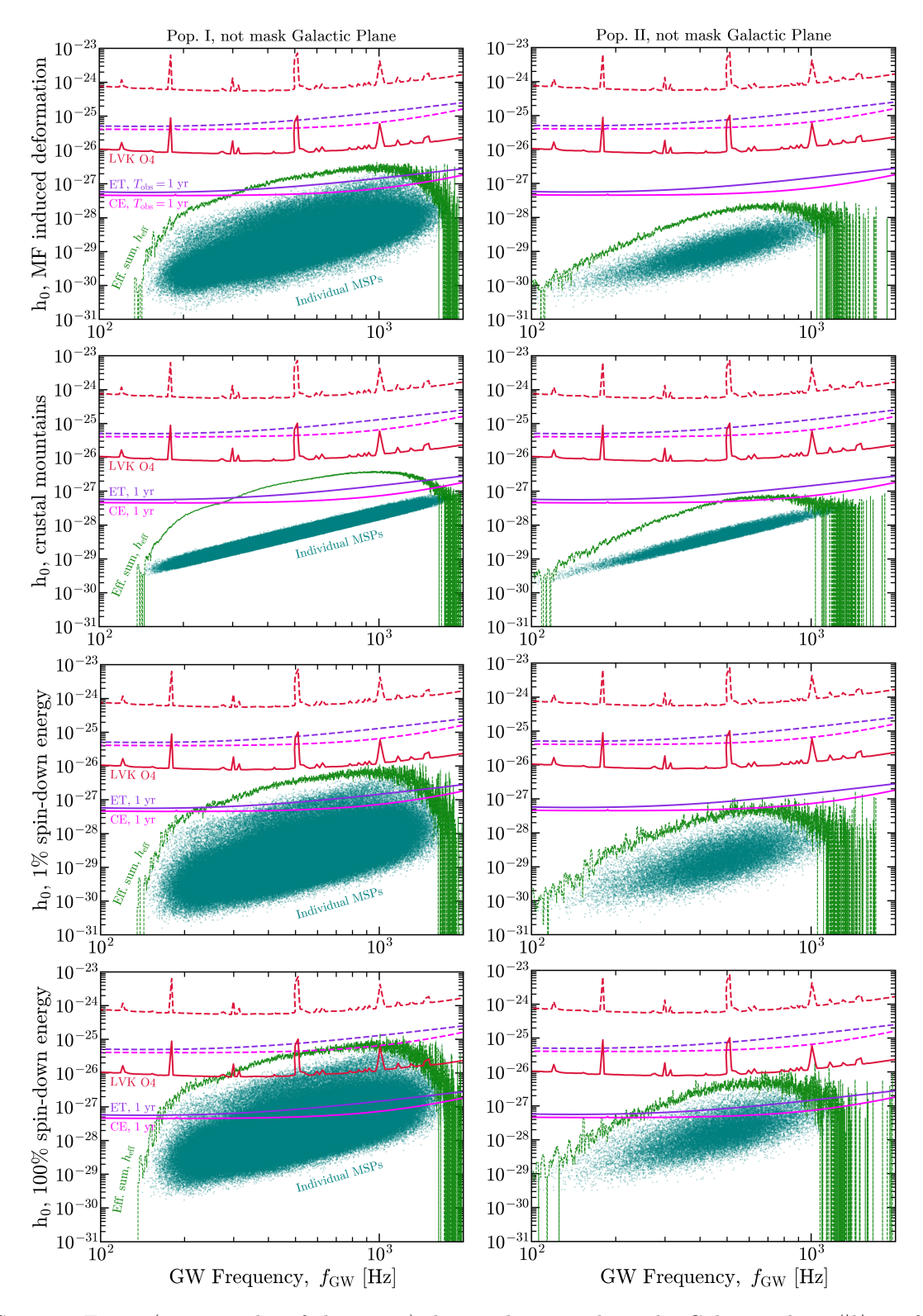


FIG. 7: Same as Fig. 3 (main results of the paper), but without masking the Galactic plane ( $|b| < 2^{\circ}$ ), i.e., corresponding to the region  $|\ell| < 20^{\circ}$ ,  $|b| < 20^{\circ}$ . The Galactic plane causes significant contamination in gamma-ray detection, but may not pose a problem for GW detection. Including  $|b| < 2^{\circ}$  and  $|\ell| < 20^{\circ}$  increases the total number of MSPs ( $N_{\rm MSP}$ ) by 70%, resulting in a modest improvement in GW detectability. See text for details.

- [1] V. C. Rubin, N. Thonnard, and W. K. Ford, Jr., "Rotational properties of 21 SC galaxies with a large range of luminosities and radii, from NGC 4605 /R = 4kpc/to UGC 2885 /R = 122 kpc/," Astrophys. J. 238, 471 (1980).
- [2] A. Bosma, "21-cm line studies of spiral galaxies. 2. The distribution and kinematics of neutral hydrogen in spiral galaxies of various morphological types." Astron. J. 86, 1825 (1981).
- [3] Edvige Corbelli and Paolo Salucci, "The Extended Rotation Curve and the Dark Matter Halo of M33," Mon. Not. Roy. Astron. Soc. 311, 441–447 (2000), arXiv:astro-ph/9909252.
- [4] Douglas Clowe, Anthony Gonzalez, and Maxim Markevitch, "Weak-lensing mass reconstruction of the interacting cluster 1e 0657-558: Direct evidence for the existence of dark matter," The Astrophysical Journal 604, 596-603 (2004).
- [5] Douglas Clowe, Marusa Bradac, Anthony H. Gonzalez, Maxim Markevitch, Scott W. Randall, Christine Jones, and Dennis Zaritsky, "A direct empirical proof of the existence of dark matter," Astrophys. J. Lett. 648, L109– L113 (2006), arXiv:astro-ph/0608407.
- [6] Daniel J. Eisenstein et al. (SDSS), "Detection of the Baryon Acoustic Peak in the Large-Scale Correlation Function of SDSS Luminous Red Galaxies," Astrophys. J. 633, 560-574 (2005), arXiv:astro-ph/0501171.
- [7] Volker Springel, Carlos S. Frenk, and Simon D. M. White, "The large-scale structure of the Universe," Nature 440, 1137 (2006), arXiv:astro-ph/0604561.
- [8] G. Hinshaw et al. (WMAP), "Nine-Year Wilkinson Microwave Anisotropy Probe (WMAP) Observations: Cosmological Parameter Results," Astrophys. J. Suppl. 208, 19 (2013), arXiv:1212.5226 [astro-ph.CO].
- [9] N. Aghanim et al. (Planck), "Planck 2018 results. VI. Cosmological parameters," Astron. Astrophys. 641, A6 (2020), [Erratum: Astron.Astrophys. 652, C4 (2021)], arXiv:1807.06209 [astro-ph.CO].
- [10] Gerard Jungman, Marc Kamionkowski, and Kim Griest, "Supersymmetric dark matter," Phys. Rept. 267, 195–373 (1996), arXiv:hep-ph/9506380.
- [11] Gianfranco Bertone and Dan Hooper, "History of dark matter," Rev. Mod. Phys. 90, 045002 (2018), arXiv:1605.04909 [astro-ph.CO].
- [12] Marco Cirelli, Alessandro Strumia, and Jure Zupan, "Dark Matter," (2024), arXiv:2406.01705 [hep-ph].
- [13] Esra Bulbul, Maxim Markevitch, Adam Foster, Randall K. Smith, Michael Loewenstein, and Scott W. Randall, "Detection of An Unidentified Emission Line in the Stacked X-ray spectrum of Galaxy Clusters," Astrophys. J. 789, 13 (2014), arXiv:1402.2301 [astro-ph.CO].
- [14] M. Ackermann et al. (Fermi-LAT), "Searching for Dark Matter Annihilation from Milky Way Dwarf Spheroidal Galaxies with Six Years of Fermi Large Area Telescope Data," Phys. Rev. Lett. 115, 231301 (2015), arXiv:1503.02641 [astro-ph.HE].
- [15] Morad Aaboud *et al.* (ATLAS), "Search for dark matter at  $\sqrt{s} = 13$  TeV in final states containing an energetic photon and large missing transverse momentum with the ATLAS detector," Eur. Phys. J. C 77, 393 (2017), arXiv:1704.03848 [hep-ex].

- [16] N. Du et al. (ADMX), "A Search for Invisible Axion Dark Matter with the Axion Dark Matter Experiment," Phys. Rev. Lett. 120, 151301 (2018), arXiv:1804.05750 [hep-ex].
- [17] Julien Billard et al., "Direct detection of dark matter—APPEC committee report\*," Rept. Prog. Phys. 85, 056201 (2022), arXiv:2104.07634 [hep-ex].
- [18] Yue Meng et al. (PandaX-4T), "Dark Matter Search Results from the PandaX-4T Commissioning Run," Phys. Rev. Lett. 127, 261802 (2021), arXiv:2107.13438 [hepex].
- [19] Haipeng An, Shuailiang Ge, Wen-Qing Guo, Xiaoyuan Huang, Jia Liu, and Zhiyao Lu, "Direct Detection of Dark Photon Dark Matter Using Radio Telescopes," Phys. Rev. Lett. 130, 181001 (2023), arXiv:2207.05767 [hep-ph].
- [20] Wen-Qing Guo, Yichao Li, Xiaoyuan Huang, Yin-Zhe Ma, Geoff Beck, Yogesh Chandola, and Feng Huang, "Constraints on dark matter annihilation from the FAST observation of the Coma Berenices dwarf galaxy," Phys. Rev. D 107, 103011 (2023), arXiv:2209.15590 [astro-ph.HE].
- [21] J. Aalbers et al. (LZ), "First Dark Matter Search Results from the LUX-ZEPLIN (LZ) Experiment," Phys. Rev. Lett. 131, 041002 (2023), arXiv:2207.03764 [hepex].
- [22] E. Aprile et al. (XENON), "First Dark Matter Search with Nuclear Recoils from the XENONnT Experiment," Phys. Rev. Lett. 131, 041003 (2023), arXiv:2303.14729 [hep-ex].
- [23] Zhen Cao et al. (LHAASO), "Constraints on Ultraheavy Dark Matter Properties from Dwarf Spheroidal Galaxies with LHAASO Observations," Phys. Rev. Lett. 133, 061001 (2024), arXiv:2406.08698 [astro-ph.HE].
- [24] Lisa Goodenough and Dan Hooper, "Possible Evidence For Dark Matter Annihilation In The Inner Milky Way From The Fermi Gamma Ray Space Telescope," (2009), arXiv:0910.2998 [hep-ph].
- [25] Oscar Macias and Chris Gordon, "Contribution of cosmic rays interacting with molecular clouds to the Galactic Center gamma-ray excess," Phys. Rev. D 89, 063515 (2014), arXiv:1312.6671 [astro-ph.HE].
- [26] Kevork N. Abazajian, Nicolas Canac, Shunsaku Horiuchi, and Manoj Kaplinghat, "Astrophysical and Dark Matter Interpretations of Extended Gamma-Ray Emission from the Galactic Center," Phys. Rev. D 90, 023526 (2014), arXiv:1402.4090 [astro-ph.HE].
- [27] Bei Zhou, Yun-Feng Liang, Xiaoyuan Huang, Xiang Li, Yi-Zhong Fan, Lei Feng, and Jin Chang, "GeV excess in the Milky Way: The role of diffuse galactic gamma-ray emission templates," Phys. Rev. D 91, 123010 (2015), arXiv:1406.6948 [astro-ph.HE].
- [28] Francesca Calore, Ilias Cholis, and Christoph Weniger, "Background Model Systematics for the Fermi GeV Excess," JCAP 03, 038 (2015), arXiv:1409.0042 [astro-ph.CO].
- [29] Xiaoyuan Huang, Torsten Enßlin, and Marco Selig, "Galactic dark matter search via phenomenological astrophysics modeling," JCAP **04**, 030 (2016), arXiv:1511.02621 [astro-ph.HE].
- [30] M. Ackermann et al. (Fermi-LAT), "The Fermi Galactic

- Center GeV Excess and Implications for Dark Matter," Astrophys. J. **840**, 43 (2017), arXiv:1704.03910 [astroph.HE].
- [31] Yi-Ming Zhong, Samuel D. McDermott, Ilias Cholis, and Patrick J. Fox, "Testing the Sensitivity of the Galactic Center Excess to the Point Source Mask," Phys. Rev. Lett. 124, 231103 (2020), arXiv:1911.12369 [astro-ph.HE].
- [32] Îlias Cholis, Yi-Ming Zhong, Samuel D. McDermott, and Joseph P. Surdutovich, "Return of the templates: Revisiting the Galactic Center excess with multimessenger observations," Phys. Rev. D 105, 103023 (2022), arXiv:2112.09706 [astro-ph.HE].
- [33] Yi-Ming Zhong and Ilias Cholis, "Robustness of the Galactic Center excess morphology against masking," Phys. Rev. D 109, 123017 (2024), arXiv:2401.02481 [astro-ph.HE].
- [34] Deheng Song, Christopher Eckner, Chris Gordon, Francesca Calore, Oscar Macias, Kevork N. Abazajian, Shunsaku Horiuchi, Manoj Kaplinghat, and Martin Pohl, "Robust inference of the Galactic Centre gammaray excess spatial properties," Mon. Not. Roy. Astron. Soc. 530, 4395–4411 (2024), arXiv:2402.05449 [astroph.GA].
- [35] Dan Hooper and Lisa Goodenough, "Dark Matter Annihilation in The Galactic Center As Seen by the Fermi Gamma Ray Space Telescope," Phys. Lett. B **697**, 412–428 (2011), arXiv:1010.2752 [hep-ph].
- [36] Tansu Daylan, Douglas P. Finkbeiner, Dan Hooper, Tim Linden, Stephen K. N. Portillo, Nicholas L. Rodd, and Tracy R. Slatyer, "The Characterization of the Gamma-Ray Signal from the Central Milky Way: A Case for Annihilating Dark Matter," Phys. Dark Univ. 12, 1–23 (2016), arXiv:1402.6703 [astro-ph.HE].
- [37] Francesca Calore, Ilias Cholis, Christopher McCabe, and Christoph Weniger, "A Tale of Tails: Dark Matter Interpretations of the Fermi GeV Excess in Light of Background Model Systematics," Phys. Rev. D 91, 063003 (2015), arXiv:1411.4647 [hep-ph].
- [38] Prateek Agrawal, Brian Batell, Patrick J. Fox, and Roni Harnik, "WIMPs at the Galactic Center," JCAP 05, 011 (2015), arXiv:1411.2592 [hep-ph].
- [39] Eder Izaguirre, Gordan Krnjaic, and Brian Shuve, "The Galactic Center Excess from the Bottom Up," Phys. Rev. D 90, 055002 (2014), arXiv:1404.2018 [hep-ph].
- [40] Rebecca K. Leane and Tracy R. Slatyer, "Revival of the Dark Matter Hypothesis for the Galactic Center Gamma-Ray Excess," Phys. Rev. Lett. 123, 241101 (2019), arXiv:1904.08430 [astro-ph.HE].
- [41] Simona Murgia, "The Fermi-LAT Galactic Center Excess: Evidence of Annihilating Dark Matter?" Ann. Rev. Nucl. Part. Sci. 70, 455-483 (2020).
- [42] Kevork N. Abazajian, "The Consistency of Fermi-LAT Observations of the Galactic Center with a Millisecond Pulsar Population in the Central Stellar Cluster," JCAP 03, 010 (2011), arXiv:1011.4275 [astro-ph.HE].
- [43] Qiang Yuan and Bing Zhang, "Millisecond pulsar interpretation of the Galactic center gamma-ray excess," JHEAp 3-4, 1-8 (2014), arXiv:1404.2318 [astro-ph.HE].
- [44] Jovana Petrović, Pasquale D. Serpico, and Gabrijela Zaharijas, "Millisecond pulsars and the Galactic Center gamma-ray excess: the importance of luminosity function and secondary emission," JCAP **02**, 023 (2015), arXiv:1411.2980 [astro-ph.HE].

- [45] Samuel K. Lee, Mariangela Lisanti, Benjamin R. Safdi, Tracy R. Slatyer, and Wei Xue, "Evidence for Unresolved γ-Ray Point Sources in the Inner Galaxy," Phys. Rev. Lett. 116, 051103 (2016), arXiv:1506.05124 [astroph.HE].
- [46] Richard Bartels, Suraj Krishnamurthy, and Christoph Weniger, "Strong support for the millisecond pulsar origin of the Galactic center GeV excess," Phys. Rev. Lett. 116, 051102 (2016), arXiv:1506.05104 [astro-ph.HE].
- [47] Oscar Macias, Chris Gordon, Roland M. Crocker, Brenna Coleman, Dylan Paterson, Shunsaku Horiuchi, and Martin Pohl, "Galactic bulge preferred over dark matter for the Galactic centre gamma-ray excess," Nature Astron. 2, 387–392 (2018), arXiv:1611.06644 [astroph.HE].
- [48] Richard Bartels, Emma Storm, Christoph Weniger, and Francesca Calore, "The Fermi-LAT GeV excess as a tracer of stellar mass in the Galactic bulge," Nature Astron. 2, 819–828 (2018), arXiv:1711.04778 [astro-ph.HE].
- [49] Anuj Gautam, Roland M. Crocker, Lilia Ferrario, Ashley J. Ruiter, Harrison Ploeg, Chris Gordon, and Oscar Macias, "Millisecond pulsars from accretion-induced collapse as the origin of the Galactic Centre gammaray excess signal," Nature Astron. 6, 703–707 (2022), arXiv:2106.00222 [astro-ph.HE].
- [50] M. A. Alpar, A. F. Cheng, M. A. Ruderman, and J. Shaham, "A new class of radio pulsars," Nature (London) 300, 728–730 (1982).
- [51] D Bhattacharya and E.P.J van den Heuvel, "Formation and evolution of binary and millisecond radio pulsars," Physics Reports 203, 1–124 (1991).
- [52] D. R. Lorimer, "Binary and Millisecond Pulsars," Living Rev. Rel. 11, 8 (2008), arXiv:0811.0762 [astro-ph].
- [53] Oleg Y. Gnedin, Jeremiah P. Ostriker, and Scott Tremaine, "Co-Evolution of Galactic Nuclei and Globular Cluster Systems," Astrophys. J. 785, 71 (2014), arXiv:1308.0021 [astro-ph.CO].
- [54] Manuel Arca-Sedda and Roberto Capuzzo-Dolcetta, "The Globular Cluster Migratory Origin of Nuclear Star Clusters," Mon. Not. Roy. Astron. Soc. 444, 3738–3755 (2014), arXiv:1405.7593 [astro-ph.GA].
- [55] Timothy D. Brandt and Bence Kocsis, "Disrupted Globular Clusters Can Explain the Galactic Center Gamma Ray Excess," Astrophys. J. 812, 15 (2015), arXiv:1507.05616 [astro-ph.HE].
- [56] Jean-Pierre Macquart and Nissim Kanekar, "On Detecting Millisecond Pulsars at the Galactic Center," Astrophys. J. 805, 172 (2015), arXiv:1504.02492 [astroph.HE].
- [57] Marcus E. Lower, Shi Dai, Simon Johnston, and Ewan D. Barr, "A Millisecond Pulsar Binary Embedded in a Galactic Center Radio Filament," Astrophys. J. Lett. 967, L16 (2024), arXiv:2404.09098 [astro-ph.HE].
- [58] M. Ajello et al. (Fermi-LAT), "Fermi Large Area Telescope Performance after 10 Years of Operation," Astrophys. J. Supp. 256, 12 (2021), arXiv:2106.12203 [astroph.IM].
- [59] Harrison Ploeg, Chris Gordon, Roland Crocker, and Oscar Macias, "Comparing the galactic bulge and galactic disk millisecond pulsars," Journal of Cosmology and Astroparticle Physics 2020, 035–035 (2020).
- [60] Ian Holst and Dan Hooper, "New determination of the millisecond pulsar gamma-ray luminosity function and

- implications for the Galactic Center gamma-ray excess," Phys. Rev. D **111**, 023048 (2025), arXiv:2403.00978 [astro-ph.HE].
- [61] James M. Cordes and T. J. W. Lazio, "NE2001. 1. A New model for the galactic distribution of free electrons and its fluctuations," (2002), arXiv:astro-ph/0207156.
- [62] K. Stovall, D. R. Lorimer, and R. S. Lynch, "Searching for millisecond pulsars: surveys, techniques and prospects," Classical and Quantum Gravity 30, 224003 (2013), arXiv:1308.4612 [astro-ph.GA].
- [63] Francesca Calore, Mattia Di Mauro, Fiorenza Donato, Jason W. T. Hessels, and Christoph Weniger, "Radio detection prospects for a bulge population of millisecond pulsars as suggested by Fermi LAT observations of the inner Galaxy," Astrophys. J. 827, 143 (2016), arXiv:1512.06825 [astro-ph.HE].
- [64] Joanna Berteaud, Francesca Calore, Maica Clavel, Pasquale Dario Serpico, Guillaume Dubus, and Pierre-Olivier Petrucci, "Galactic bulge millisecond pulsars shining in x rays: A  $\gamma$ -ray perspective," Phys. Rev. D **104**, 043007 (2021), arXiv:2012.03580 [astro-ph.HE].
- [65] J. Berteaud, F. Calore, M. Clavel, J. Marvil, S. Hyman, F. K. Schinzel, and M. Kerr, "Multiwavelength identification of millisecond pulsar candidates in the Galactic bulge," Astron. Astrophys. 690, A330 (2024).
- [66] In addition, the mHz band of the Laser Interferometer Space Antenna could also probe those MSPs in the binary systems; see Ref. [133] for a recent study.
- [67] J. Aasi et al. (LIGO Scientific), "Advanced LIGO," Class. Quant. Grav. 32, 074001 (2015), arXiv:1411.4547 [gr-qc].
- [68] F. Acernese et al. (VIRGO), "Advanced Virgo: a second-generation interferometric gravitational wave detector," Class. Quant. Grav. 32, 024001 (2015), arXiv:1408.3978 [gr-qc].
- [69] T. Akutsu et al. (KAGRA), "KAGRA: 2.5 Generation Interferometric Gravitational Wave Detector," Nature Astron. 3, 35–40 (2019), arXiv:1811.08079 [gr-qc].
- [70] Matthew Evans et al., "Cosmic Explorer: A Submission to the NSF MPSAC ngGW Subcommittee," (2023), arXiv:2306.13745 [astro-ph.IM].
- [71] M. Punturo et al., "The Einstein Telescope: A third-generation gravitational wave observatory," Class. Quant. Grav. 27, 194002 (2010).
- [72] Francesca Calore, Tania Regimbau, and Pasquale Dario Serpico, "Probing the Fermi-LAT GeV excess with gravitational waves," Phys. Rev. Lett. 122, 081103 (2019), arXiv:1812.05094 [astro-ph.HE].
- [73] Andrew L. Miller and Yue Zhao, "Probing the Pulsar Explanation of the Galactic-Center GeV Excess Using Continuous Gravitational-Wave Searches," Phys. Rev. Lett. **131**, 081401 (2023), arXiv:2301.10239 [astroph.HE].
- [74] Kayla Bartel and Stefano Profumo, "Gravitational wave counterpart to a gamma-ray Galactic Center signal from millisecond pulsars," Phys. Rev. D 110, 123036 (2024), arXiv:2409.12271 [astro-ph.HE].
- [75] As a complementary avenue to ground-based interferometers, a recent proposal suggests probing kHz-band backgrounds using a laser-polarization "Gravitational Photon Polarization Twist" in space [134]. With optimistic baselines (~ 10<sup>6</sup> km) and millisecond pulses, its reach could overlap the collective strains expected from a bulge MSP population [134].

- [76] Varun Srivastava, Derek Davis, Kevin Kuns, Philippe Landry, Stefan Ballmer, Matthew Evans, Evan D. Hall, Jocelyn Read, and B. S. Sathyaprakash, "Sciencedriven Tunable Design of Cosmic Explorer Detectors," Astrophys. J. 931, 22 (2022), arXiv:2201.10668 [gr-qc].
- [77] Stefan Hild, Simon Chelkowski, and Andreas Freise, "Pushing towards the ET sensitivity using 'conventional' technology," (2008), arXiv:0810.0604 [gr-qc].
- [78] E. Capote et al., "Advanced LIGO detector performance in the fourth observing run," Phys. Rev. D 111, 062002 (2025), arXiv:2411.14607 [gr-qc].
- [79] A. G. Abac et al. (LIGO Scientific, VIRGO, KA-GRA), "Search for Continuous Gravitational Waves from Known Pulsars in the First Part of the Fourth LIGO-Virgo-KAGRA Observing Run," Astrophys. J. 983, 99 (2025), arXiv:2501.01495 [astro-ph.HE].
- [80] Michele Maggiore, Gravitational Waves. Vol. 1: Theory and Experiments (Oxford University Press, 2007).
- [81] G. Woan, M. D. Pitkin, B. Haskell, D. I. Jones, and P. D. Lasky, "Evidence for a Minimum Ellipticity in Millisecond Pulsars," Astrophys. J. Lett. 863, L40 (2018), arXiv:1806.02822 [astro-ph.HE].
- [82] S. Chandrasekhar and E. Fermi, "Problems of Gravitational Stability in the Presence of a Magnetic Field," Astrophys. J. 118, 116 (1953), [Erratum: Astrophys.J. 122, 208 (1955)].
- [83] Michele Maggiore, Gravitational Waves. Vol. 2: Astrophysics and Cosmology (Oxford University Press, 2018).
- [84] A.B. Migdal, "Superfluidity and the moments of inertia of nuclei," Nuclear Physics 13, 655–674 (1959).
- [85] Gordon Baym, Christopher Pethick, David Pines, and Malvin Ruderman, "Spin Up in Neutron Stars: The Future of the Vela Pulsar," Nature (London) 224, 872– 874 (1969).
- [86] Curt Cutler, "Gravitational waves from neutron stars with large toroidal B fields," Phys. Rev. D 66, 084025 (2002), arXiv:gr-qc/0206051.
- [87] Taner Akgun and Ira Wasserman, "Toroidal Magnetic Fields in Type II Superconducting Neutron Stars," Mon. Not. Roy. Astron. Soc. 383, 1551–1580 (2008), arXiv:0705.2195 [astro-ph].
- [88] S. K. Lander, N. Andersson, and K. Glampedakis, "Magnetic neutron star equilibria with stratification and type ii superconductivity: Stratified and superconducting ns equilibria," Monthly Notices of the Royal Astronomical Society 419, 732–747 (2011).
- [89] S. K. Lander, "The contrasting magnetic fields of superconducting pulsars and magnetars," Mon. Not. Roy. Astron. Soc. 437, 424–436 (2014), arXiv:1307.7020 [astroph.HE].
- [90] R. Abbott et al. (LIGO Scientific, Virgo), "Gravitational-wave Constraints on the Equatorial Ellipticity of Millisecond Pulsars," Astrophys. J. Lett. 902, L21 (2020), arXiv:2007.14251 [astro-ph.HE].
- [91] Alpha Mastrano and Andrew Melatos, "Updated gravitational-wave upper limits on the internal magnetic field strength of recycled pulsars," Mon. Not. Roy. Astron. Soc. 421, 760 (2012), arXiv:1112.1542 [astroph.HE].
- [92] Riccardo Ciolfi and Luciano Rezzolla, "Twisted-torus configurations with large toroidal magnetic fields in relativistic stars," Mon. Not. Roy. Astron. Soc. 435, L43– L47 (2013), arXiv:1306.2803 [astro-ph.SR].
- [93] B. Haskell, Maxim Priymak, Alessandro Patruno,

- Manuel Oppenoorth, Andrew Melatos, and Paul D. Lasky, "Detecting gravitational waves from mountains on neutron stars in the Advanced Detector Era," Mon. Not. Roy. Astron. Soc. **450**, 2393–2403 (2015), arXiv:1501.06039 [astro-ph.SR].
- [94] Anatoly Spitkovsky, "Time-dependent force-free pulsar magnetospheres: axisymmetric and oblique rotators," Astrophys. J. Lett. 648, L51–L54 (2006), arXiv:astro-ph/0603147.
- [95] Greg Ushomirsky, Curt Cutler, and Lars Bildsten, "Deformations of accreting neutron star crusts and gravitational wave emission," Mon. Not. Roy. Astron. Soc. 319, 902 (2000), arXiv:astro-ph/0001136.
- [96] Benjamin J. Owen, "Maximum elastic deformations of compact stars with exotic equations of state," Phys. Rev. Lett. 95, 211101 (2005), arXiv:astro-ph/0503399.
- [97] N. Andersson, V. Ferrari, D. I. Jones, K. D. Kokkotas, B. Krishnan, J. S. Read, L. Rezzolla, and B. Zink, "Gravitational waves from neutron stars: promises and challenges," General Relativity and Gravitation 43, 409–436 (2010).
- [98] Nathan K. Johnson-McDaniel and Benjamin J. Owen, "Maximum elastic deformations of relativistic stars," Phys. Rev. D 88, 044004 (2013), arXiv:1208.5227 [astro-ph.SR].
- [99] C. J. Horowitz and Kai Kadau, "The Breaking Strain of Neutron Star Crust and Gravitational Waves," Phys. Rev. Lett. 102, 191102 (2009), arXiv:0904.1986 [astro-ph.SR].
- [100] A. I. Chugunov and C. J. Horowitz, "Breaking stress of neutron star crust," Mon. Not. Roy. Astron. Soc. 407, L54-L58 (2010), arXiv:1006.2279 [astro-ph.SR].
- [101] J. A. Morales and C. J. Horowitz, "Limiting Rotation Rate of Neutron Stars from Crust Breaking and Gravitational Waves," Astrophys. J. Lett. 978, L8 (2025), arXiv:2410.19111 [astro-ph.HE].
- [102] J. A. Morales and C. J. Horowitz, "Finite-Element Simulations of Rotating Neutron Stars with Anisotropic Crusts and Continuous Gravitational Waves," (2024), arXiv:2409.14482 [gr-qc].
- [103] R. Abbott et al. (KAGRA, LIGO Scientific, VIRGO), "Search for continuous gravitational wave emission from the Milky Way center in O3 LIGO-Virgo data," Phys. Rev. D 106, 042003 (2022), arXiv:2204.04523 [astro-ph.HE].
- [104] R N Manchester, G B Hobbs, A Teoh, and M Hobbs, "The Australia Telescope National Facility pulsar catalogue," Astron. J. 129, 1993 (2005), arXiv:astroph/0412641.
- [105] Roland M. Crocker et al., "Diffuse Galactic antimatter from faint thermonuclear supernovae in old stellar populations," (2016), 10.1038/s41550-017-0135, arXiv:1607.03495 [astro-ph.HE].
- [106] Florian List, Yujin Park, Nicholas L. Rodd, Eve Schoen, and Florian Wolf, "On the Energy Distribution of the Galactic Center Excess' Sources," (2025), arXiv:2507.17804 [astro-ph.HE].
- [107] P. C. C. Freire et al., "Long-term observations of the pulsars in 47 Tucanae – II. Proper motions, accelerations and jerks," Mon. Not. Roy. Astron. Soc. 471, 857–876 (2017), arXiv:1706.04908 [astro-ph.HE].
- [108] R. Abbott et al. (KAGRA, LIGO Scientific, VIRGO), "All-sky search for continuous gravitational waves from isolated neutron stars using Advanced LIGO and Ad-

- vanced Virgo O3 data," Phys. Rev. D **106**, 102008 (2022), arXiv:2201.00697 [gr-qc].
- [109] I. S. Shklovskii, "Possible Causes of the Secular Increase in Pulsar Periods." Soviet Astronomy 13, 562 (1970).
- [110] Thibault Damour and Joseph H. Taylor, "On the orbital period change of the binary pulsar PSR-1913+16," Astrophys. J. 366, 501-511 (1991).
- [111] The KDE method can be found in the documentation: https://docs.scipy.org/doc/scipy/reference/ generated/scipy.stats.gaussian\_kde.html.
- [112] See also Ref. [135] for a recent study, which shows that realistic MW simulations yield a flattened, boxy DM distribution, making the GCE morphology from WIMP annihilation hard to distinguish from that of MSPs.
- [113] H. T. Freudenreich, "A COBE Model of the Galactic Bar and Disk," Astrophys. J. 492, 495–510 (1998), arXiv:astro-ph/9707340 [astro-ph].
- [114] Oscar Macias, Shunsaku Horiuchi, Manoj Kaplinghat, Chris Gordon, Roland M. Crocker, and David M. Nataf, "Strong evidence that the galactic bulge is shining in gamma rays," Journal of Cosmology and Astroparticle Physics 2019, 042 (2019).
- [115] Jack T. Dinsmore and Tracy R. Slatyer, "Luminosity functions consistent with a pulsar-dominated Galactic Center excess," JCAP 06, 025 (2022), arXiv:2112.09699 [astro-ph.HE].
- [116] Julio F. Navarro, Carlos S. Frenk, and Simon D. M. White, "The Structure of cold dark matter halos," Astrophys. J. 462, 563–575 (1996), arXiv:astroph/9508025.
- [117] HongSheng Zhao, "Analytical models for galactic nuclei," Mon. Not. Roy. Astron. Soc. 278, 488–496 (1996), arXiv:astro-ph/9509122.
- [118] Julio F. Navarro, Carlos S. Frenk, and Simon D. M. White, "A Universal density profile from hierarchical clustering," Astrophys. J. 490, 493–508 (1997), arXiv:astro-ph/9611107.
- [119] R. Abbott et al. (KAGRA, VIRGO, LIGO Scientific), "All-sky search for continuous gravitational waves from isolated neutron stars in the early O3 LIGO data," Phys. Rev. D 104, 082004 (2021), arXiv:2107.00600 [gr-qc].
- [120] P. B. Covas, M. A. Papa, R. Prix, and B. J. Owen, "Constraints on r-modes and Mountains on Millisecond Neutron Stars in Binary Systems," Astrophys. J. Lett. 929, L19 (2022), arXiv:2203.01773 [gr-qc].
- [121] The sensitivity curves for LVK O4 are adopted from Ref. [79]. The PSD data files for CE (with the baseline 40 km detector) and ET (with option ET-B) are available for download at https://dcc.cosmicexplorer.org/CE-T2000017/public and https://www.et-gw.eu/index.php/etsensitivities, respectively.
- [122] Despite not being a member of the MSP population involved in our Pop. I samples, it remains a promising candidate for targeted GW searches [79, 136–138].
- [123] I. Yusifov and I. Kucuk, "Revisiting the radial distribution of pulsars in the galaxy," Astron. Astrophys. 422, 545–553 (2004), arXiv:astro-ph/0405559.
- [124] D. R. Lorimer et al., "The Parkes multibeam pulsar survey: VI. Discovery and timing of 142 pulsars and a Galactic population analysis," Mon. Not. Roy. Astron. Soc. 372, 777–800 (2006), arXiv:astro-ph/0607640.
- [125] M. Ackermann et al. (Fermi-LAT), "An extremely

- bright gamma-ray pulsar in the Large Magellanic Cloud," Science **350**, 801–805 (2015).
- [126] A. Abramowski et al. (H.E.S.S.), "Discovery of gammaray emission from the extragalactic pulsar wind nebula N157B with the High Energy Stereoscopic System," Astron. Astrophys. 545, L2 (2012), arXiv:1208.1636 [astro-ph.HE].
- [127] Private communication with Andrew L. Miller and Yue Zhao.
- [128] Paola Leaci and Reinhard Prix, "Directed searches for continuous gravitational waves from binary systems: Parameter-space metrics and optimal scorpius x-1 sensitivity," Physical Review D 91 (2015), 10.1103/physrevd.91.102003.
- [129] Paola Leaci, Pia Astone, Sabrina D'Antonio, Sergio Frasca, Cristiano Palomba, Ornella Piccinni, and Simone Mastrogiovanni, "Novel directed search strategy to detect continuous gravitational waves from neutron stars in low- and high-eccentricity binary systems," Phys. Rev. D 95, 122001 (2017), arXiv:1607.08751 [astro-ph.IM].
- [130] B. P. Abbott et al. (LIGO Scientific, Virgo), "All-sky search for continuous gravitational waves from isolated neutron stars using Advanced LIGO O2 data," Phys. Rev. D 100, 024004 (2019), arXiv:1903.01901 [astro-ph.HE].
- [131] James Binney, Ortwin Gerhard, and David Spergel, "The photometric structure of the inner galaxy," Mon. Not. Roy. Astron. Soc. 288, 365–374 (1997), arXiv:astro-ph/9609066.
- [132] E. Vanhollebeke, M. A. T. Groenewegen, and L. Gi-

- rardi, "Stellar populations in the galactic bulge: Modelling the galactic bulge with trilegal," Astronomy & Astrophysics 498, 95–107 (2009).
- [133] Valeriya Korol and Andrei Igoshev, "Probing the millisecond pulsar origin of the GeV excess in the Galactic Centre with LISA," (2025), arXiv:2509.12998 [astro-ph.HE].
- [134] Rodolfo Capdevilla, "Gravitational Photon Polarization Twist to Probe the Early Universe and the Galactic Center," (2025), arXiv:2507.05347 [hep-ph].
- [135] Moorits Mihkel Muru, Joseph Silk, Noam I. Libeskind, Stefan Gottloeber, and Yehuda Hoffman, "Fermi-LAT Galactic Center Excess Morphology of Dark Matter in Simulations of the Milky Way Galaxy," Phys. Rev. Lett. 135, 161005 (2025), arXiv:2508.06314 [astro-ph.HE].
- [136] Liudmila Fesik and Maria Alessandra Papa, "First Search for r-mode Gravitational Waves from PSR J0537-6910," Astrophys. J. 895, 11 (2020), [Erratum: Astrophys.J. 897, 185 (2020)], arXiv:2001.07605 [gr-qc].
- [137] R. Abbott *et al.* (LIGO Scientific, Virgo, KAGRA), "Constraints from LIGO O3 Data on Gravitational-wave Emission Due to R-modes in the Glitching Pulsar PSR J0537–6910," Astrophys. J. **922**, 71 (2021), arXiv:2104.14417 [astro-ph.HE].
- [138] R. Abbott et al. (LIGO Scientific, Virgo, KAGRA), "Diving below the Spin-down Limit: Constraints on Gravitational Waves from the Energetic Young Pulsar PSR J0537-6910," Astrophys. J. 913, L27 (2021), arXiv:2012.12926 [astro-ph.HE].